SEMMELWEIS EGYETEM DOKTORI ISKOLA

Ph.D. értekezések

3298.

HAJDÚ BENCE

Patobiokémia

című program

Programvezető: Dr. Csala Miklós, egyetemi tanár

Témavezető: Dr. Mészáros-Kapuy Orsolya, egyetemi docens

Systems Biological Analysis of mTOR-Dependent Molecular Mechanisms of Autophagy

PhD thesis

HAJDÚ BENCE

Semmelweis University Doctoral School Molecular Medicine Division





Supervisor: Orsolya Mészáros-Kapuy, Ph.D

Official reviewers: Attila Csikász-Nagy, Dsc

Miklós Cserző, Ph.D

Head of the Complex Examination Committee: Csaba Sőti, MD, D.Sc

Members of the Complex Examination Committee: Roland Csépányi-Kömi, Ph.D

János Tóth, Ph.D

Budapest, 2025

Contents

1	Intr	oductio	n		5
	1.1	Regula	ation of au	tophagy induction	6
	1.2	System	ns biology	approach	9
	1.3	In-silio	co models	of autophagy	12
2	Obj	ectives			15
3	Mat	erials a	nd metho	ds	17
	3.1	Experi	imental me	ethods	17
		3.1.1	Material	s	17
		3.1.2	Cell Cul	ture and Maintenance	17
		3.1.3	SDS-PA	GE and Western Blot Analysis	17
		3.1.4	Silencing	g with siRNA	18
		3.1.5	Treatmen	nt with inhibitors	18
		3.1.6	Statistics	8	19
	3.2	Comp	utational n	nethods	19
		3.2.1	Dynamic	cal Systems Analysis	19
		3.2.2	Computa	ational Methods for PP2A-mTORC1-ULK1 Model	20
			3.2.2.1	Mathematical Model Formulation	20
			3.2.2.2	Structural Identifiability Analysis	21
			3.2.2.3	Parameter Estimation	21
			3.2.2.4	Dynamical Systems Analysis	22
			3.2.2.5	Code Availability	22
		3.2.3	Computa	ational Methods for Autophagy Oscillation Model	22
			3.2.3.1	Mathematical Model Formulation	22
			3.2.3.2	Dynamical Systems Analysis	23
			3.2.3.3	Global Sensitivity Analysis (GSA)	23
			3.2.3.4	Code Availability	24
		3.2.4	Computa	ational Methods for Basal State Model Calibration	24

			3.2.4.1	Basal State Simulation and Error Quantification	24
			3.2.4.2	Sensitivity Analysis and Parameter Selection	25
			3.2.4.3	Parameter Optimization	26
			3.2.4.4	Posterior Uncertainty Analysis	26
			3.2.4.5	Software Implementation and Availability	26
4	Resu	ılts			27
	4.1	Parame	eterization	of a Core Autophagy Regulatory Model using Western	
		Blot Ti	me-Series	Data	27
	4.2	Oscilla	tory Dyna	amics in Autophagy Induction	30
		4.2.1	Characte	ristic of Autophagy Induction	32
		4.2.2	Requirer	nent for Model Refinement to Explain Sustained Oscilla-	
			tions in t	he AMPK-mTORC1-ULK1 Network	33
		4.2.3	A Time-l	Delayed Negative Feedback Model Reproduces Oscillations	34
		4.2.4	The Dela	y Mechanism via REG is Essential for Oscillatory Dynamics	35
	4.3	Autoph	nagy-Apop	otosis Model calibration, a Top-Down approach	36
		4.3.1	Defining	the initial concentrations	37
		4.3.2	Revision	of Incorrect Reactions	37
		4.3.3	Identifica	ation and Optimization of Influential Rate Coefficients	39
		4.3.4	Optimize	ed Model Validation and Parameter Constraints	40
5	Disc	ussion			42
	5.1	Integra	tion of Ex	sperimental Design and Computational Modeling	43
	5.2	Oscilla	tory Dyna	amics Require Time-Delayed Negative Feedback	44
	5.3	From N	Minimal M	Models to Comprehensive Networks	45
		5.3.1	Future D	virections	46
6	Conc	clusions	3		48
7	Sum	mary			50
8	Refe	rences			51
9	Bibli	ograph	y of the c	andidate's publications	67
10	Ackr	nowledg	gments		69

List of Abbreviations

AC Adenylyl cyclase
AKTA Active form of AKT

AMPK AMP-activated protein kinase
ATF4 Activating Transcription Factor 4

ATG Autophagy-related gene
ATG5t Truncated ATG5 (ATG5T)
BAX Bcl-2-associated X protein

BCL2 B-cell lymphoma 2

BCL2_BAX BCL2 and BAX complex BCL2_PUMA BCL2 and PUMA complex

BECN1 Beclin 1

BID BH3 interacting-domain death agonist

BRN Biochemical reaction network
CA2ER Ca ion concentration in the ER

CA2IC Ca ion in the cytoplasm

cAMP Cyclic adenosine monophosphate

CAMKK β Calcium/calmodulin-dependent protein kinase kinase 2

CHOP C/EBP homologous protein
CRN Chemical reaction network

CYTCM Cytochrome c in the mitochondria
DAPK Death associated protein kinase 1

E Error

eif 2α Eukaryotic translational initiation factor 2α

EPAC Exchange protein activated by cAMP

ER Endoplasmic Reticulum

FOCTOPUS FOCusing robusT Optimization with Uncertainty-based Sampling

GA G protein subunit α GBC G protein subunit $\beta \gamma$

GFP-LC3B Green Fluorescent Protein fused with LC3
GPCRA Active from of G protein-coupled receptor

H2B-RFP Histone H2B fused with Red Fluorescent Protein

IP3 Inositol trisphosphate

JNK Jun N-terminal kinase

L-BFGS-B Limited-memory Broyden-Fletcher-Goldfarb-Shanno with bound

LC3B Microtubule-associated proteins 1A/1B light chain 3B

LC3B-II Lipidated, membrane-bound form MAPK15 Mitogen-activated protein kinase 15

Mdm2 Mouse double minute 2 MSE Mean Squared Error

mTOR Mammalian target of rapamycin

MTORA Active mammalian target of rapamycin mTORC1 Mammalian target of rapamycin complex 1

OA Okadaic acid

ODE Ordinary differential equation
PAS Preautophagosomal structure

PERK PKR-like endoplasmic reticulum kinase PIP2 Phosphatidylinositol 4,5-bisphosphate

PKA Protein kinase A
PKC Protein kinase C

PLCε Inactive Phospholipase C epsilon 1

PP2A Protein phosphatase 2A

PUMA p53 upregulated modulator of apoptosis

RAP Rapamycin

REG Regulatory protein

RHEBA Active Ras Homolog Enriched In Brain

RKD ReSpecTh Kinetic Data

RMSD Root-mean-square deviation

SERCA Sarco/endoplasmic reticulum Ca²⁺-ATPase

STS Staurosporine

SUE Sensitivity, parameter uncertainty, and experimental error

tBID Truncated BH3 interacting-domain death agonist

TSC 1/2 Inactive tuberous sclerosis proteins 1 and 2 ULK1 Unc-51-like autophagy-activating kinases

UPR Unfolded protein response

UVRAG UV radiation resistance-associated gene protein

1 Introduction

Autophagy is an evolutionarily conserved cellular digestive process [1, 2], crucial for maintaining cellular homeostasis. While there are multiple forms of autophagy including chaperone-mediated autophagy, microautophagy, and macroautophagy, this study focuses exclusively on macroautophagy [3], which will be referred to simply as "autophagy" throughout this work. Autophagy is active at a basal level at all times, performing essential functions like degrading damaged proteins and aged organelles to ensure cellular quality control. Beyond this constant surveillance, autophagy has a major role as a key cellular response to external and internal stimuli, including nutrient deprivation, hypoxia, infection, or oxidative stress [1, 4, 5, 6, 7, 2]. Under these conditions, autophagy promotes cell survival by breaking down cellular material to provide essential building blocks and energy, or by eliminating harmful agents and damaged structures [8, 9, 10, 11]. Given its vital roles in the maintenance of cellular homeostasis, dysfunction in autophagy is correlated with multiple diseases, often exhibiting complex, context-dependent effects [12, 5, 13].

Research has indicated a strong correlation between irregularities in the processes of autophagy, particularly the clearance of misfolded protein aggregates, and the pathogenesis of major neurodegenerative diseases [14, 15, 16, 13]. Furthermore, impaired autophagy contributes to various metabolic disorders through dysfunction in key metabolic tissues like the liver and pancreas [17, 18, 19], and its decline is linked to aging-related conditions such as osteoarthritis and bone loss [20]. Defects have also been linked to inflammatory conditions, such as Crohn's disease [21, 22, 23], muscle atrophy [24], and complex outcomes in cardiac diseases [25, 26]. In cancers, autophagy has a dual role, serving as a tumor suppressor mechanism during early oncogenesis while simultaneously being exploited by established malignancies to enhance their survival, proliferation, metastatic potential, and therapeutic resistance [27, 28, 29, 30]. This widespread involvement across diverse pathologies underscores the considerable interest in understanding and potentially modulating this pathway for therapeutic purposes [31].

The complexity of autophagy regulation and its multifaceted roles in disease necessitate quantitative approaches like systems biology. While high-throughput omics methods are powerful for revealing system components and correlations [32, 33], understanding the

underlying dynamic mechanisms requires integrating experimental data with quantitative mathematical models [34, 35, 36]. Analyzing the dynamical properties revealed by these models, such as feedback controls, biological switches, and oscillations provides crucial mechanistic insights into how autophagy is regulated, how its dysregulation contributes to pathology, and how the system functions over time [37]. This deeper, dynamic understanding is invaluable for identifying effective therapeutic targets and predicting treatment outcomes in autophagy-related diseases [38, 39]. Accordingly, this thesis employs such a mechanistic, dynamical systems approach to investigate the core principles governing autophagy induction.

1.1 Regulation of autophagy induction

One of the most important elements of the autophagy machinery is unc51-like autophagy activating kinase 1/2 (ULK1/2) [11, 40]. ULK1/2 forms a complex with ATG13, ATG101 and FIP200 to control the autophagy induction [41, 40]. ULK1, recognized as an initiator in the autophagic process, plays important roles in activation of an autophagic response [42].

ULK1 is regulated by two important cellular growth regulators, the mammalian target of rapamycin (mTOR) and AMP-activated protein kinase (AMPK) (Figure 1.1) [43, 42]. The mTOR kinase forms two distinct signaling complexes, mTORC1 and mTORC2, by associating with various companion proteins [43]. As a key nutrient sensor, mTORC1 activity integrates multiple upstream signals; it is stimulated by abundant amino acids [44] and growth factor signaling via the phosphatidylinositol 3 kinase (PI3K)/AKT pathway [45, 46]. Additionally, mTORC1 is activated by sufficient cellular energy levels (high ATP/AMP ratio), phosphatidic acid produced by phospholipase D, and adequate oxygen availability [47, 48]. mTORC1 actively promotes protein synthesis through phosphorylation of ribosomal protein S6 kinase (p70S6K1) and translation initiation factor 4E binding protein-1 (4E-BP1) [49]. However, this activity is suppressed by the hamartin-tuberin (TSC1/2) complex, which inhibits mTORC1 and consequently blocks protein synthesis through de-phosphorylation of these downstream targets [49].

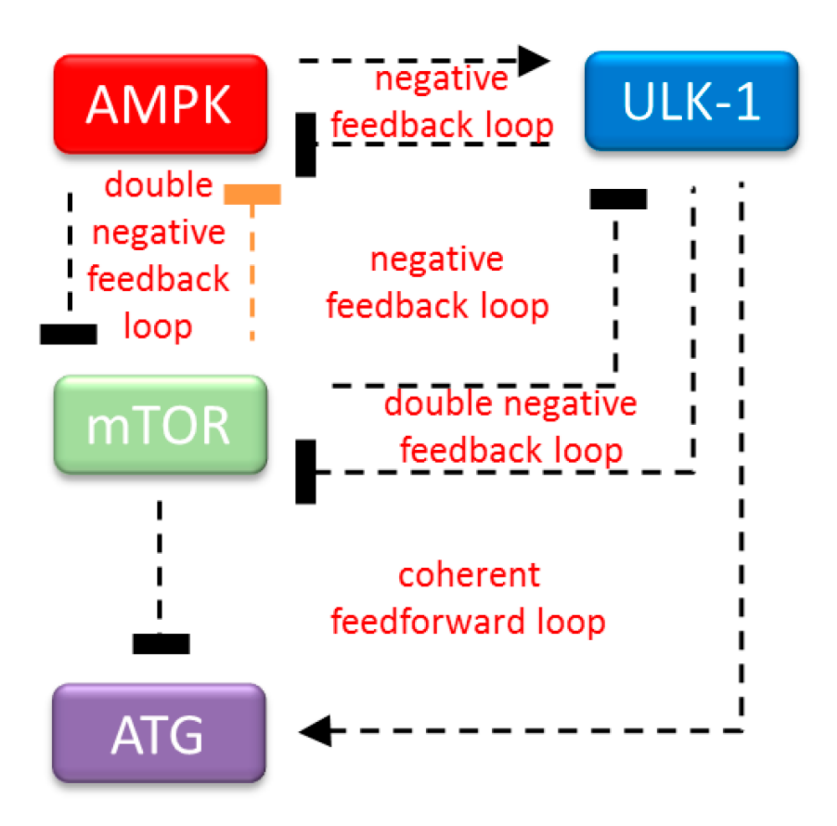


Figure 1.1: Schematic representation of the AMPK-mTORC1-ULK1 regulatory network controlling autophagy initiation. The core regulatory triangle consists of AMPK (red), mTORC1 (green), and ULK1 (blue), with downstream ATG proteins (purple) representing key autophagy initiation factors. Dashed arrows indicate positive regulatory interactions; blunt-ended lines indicate inhibitory effects. Orange highlighting denotes feedback loops identified through both experimental validation and theoretical analysis. Figure adapted from Holczer et al.[50].

AMPK, a heterotrimeric complex, acts as a crucial sensor of cellular energy homeostasis. It is primarily activated by increased intracellular AMP/ATP ratios (signifying low energy), where direct AMP binding triggers AMPK activation [8, 9, 10, 51]. AMPK restores energy homeostasis by inhibiting energy-consuming anabolic pathways (e.g., synthesis of glycogen, protein, fatty acids, and cholesterol) while promoting energy-producing catabolic pathways (e.g., glycolysis, fatty acid β -oxidation) through the Ser/Thr phosphorylation of key metabolic enzymes [8, 9, 10, 51]. Increased cytosolic Ca^{2+} concentrations due to ER stress result in calcium/calmodulin-dependent protein kinase kinase 2, beta (CAMKK2/CaMKKb) to activate AMPK. AMPK directly inhibits mTORC1 activity by phosphorylating the RAPTOR component of the mTORC1 complex [52, 53]. ULK1 is subject to antagonistic regulation by these two kinases [54, 55, 40]. During nutrient-replete conditions, mTORC1 suppresses the ULK complex through direct phosphorylation of ULK1 [55, 40]. Additionally, mTORC1 can attenuate AMPK signaling, thereby preventing

autophagy activation [51, 56]. Conversely, under conditions of energy deprivation, AMPK becomes activated and promotes autophagic self-digestion by phosphorylating ULK1 while concurrently inhibiting mTORC1 [55, 40]. The autophagic response is precisely calibrated through two distinct ULK1-mediated negative feedback mechanisms. First, ULK1 can phosphorylate and negatively regulate AMPK, thereby attenuating its own activating signal [57]. Second, ULK1 phosphorylates the RAPTOR component of mTORC1, leading to mTORC1 inhibition and sustained autophagy when nutrient limitation persists [58, 59].

As it can be seen, the regulation of autophagy through ULK1 is highly dependent on the dynamic, reversible nature of protein phosphorylation [54, 60]. Counteracting these kinases are protein phosphatases, which are essential for reversing phosphorylation and enabling precise signal control. A pivotal phosphatase in this context is Protein Phosphatase 2A (PP2A), a multi-subunit serine/threonine phosphatase typically comprising catalytic (C), scaffold (A), and variable regulatory (B) subunits [61, 62]. Beyond autophagy, PP2A plays crucial roles in maintaining broad cellular homeostasis by participating in the regulation of the cell cycle, proliferation, cell death, and diverse signaling pathways [62, 63]. Within the autophagy regulatory network, PP2A often acts antagonistically to mTORC1. While mTORC1 exerts its effect on ULK1 under nutrient-rich conditions, PP2A [64, 40, 55, 65], PP2A (frequently involving its B55-family regulatory subunit) promotes autophagy by dephosphorylating ULK1 at distinct activating sites during starvation [62, 66]. PP2A-B55 may also facilitate autophagy by dephosphorylating other key proteins like Beclin-1 and PHD2 [62, 63]. In addition to the established ULK1-mTORC1 double-negative feedback loop (where active ULK1 inhibits mTORC1 via RAPTOR phosphorylation) [40, 59, 58], a critical double-negative feedback loop also connects mTORC1 and PP2A: mTORC1 can phosphorylate and inhibit PP2A, while PP2A can inhibit mTORC1 activation by dephosphorylating upstream activators like Akt (at Thr308) [67, 68, 69]. Furthermore, ULK1 itself might positively influence PP2A activity, for instance by phosphorylating regulatory subunits like striatin, thereby establishing a positive feedback loop between ULK1 and PP2A [70].

The kinase-phosphatase balance controlling autophagy can be artificially perturbed by specific inhibitors. Rapamycin, for instance, allosterically inhibits mTORC1 by forming a complex with FKBP12 and the mTOR subunit [71]. This inhibition prevents downstream signaling, such as p70S6K1 activation [71], promotes autophagy [66], and leads to ULK1 dephosphorylation at inhibitory sites (e.g., Ser637/757) [65, 66]. Although rapamycin treatment is reported by some studies to activate AMPK (via Thr172 phosphorylation), which could then phosphorylate ULK1 (at Ser555) to further promote autophagy [50, 65, 72], this AMPK role is contested, with other reports indicating AMPK-independent autophagy induction [55] or no detectable AMPK activation [73, 74]. Inhibitors can also

target phosphatases; okadaic acid (OA) potently inhibits PP2A (and PP1 less effectively), thereby blocking key cellular dephosphorylation events [75].

Once autophagy is activated, an isolation membrane originating from the preautophagosomal structure (PAS) grows and curves through nucleation to form the autophagosome, which sequesters cytoplasmic components for degradation [76, 77, 78]. This process involves the class III phosphatidylinositol-3 kinase (PI3K) Vps34, which associates with Vps15 on the PAS membrane. Here, Beclin-1 competes with BCL-2 for Vps34 binding: the Beclin-1-Vps34 complex promotes autophagosome maturation, whereas Vps34-BCL-2 inhibits autophagy [79]. Maturation of the autophagosome requires two ubiquitin-like conjugation steps [80]. First, Atg7 activates Atg12, which is then transferred to Atg10 and covalently linked to Atg5 at Lys130. This forms the Atg5-Atg12-Atg16L complex, which promotes membrane curvature [80]. Second, LC3B is processed from its cytoplasmic form (LC3B-I) to the lipidated, membrane-bound form (LC3B-II), which integrates into both sides of the double membrane [81]. LC3B-II serves as a structural component and a receptor for selective autophagy, interacting with adaptor molecules such as p62/SQSTM1 [80]. These adaptor molecules bridge the link between ubiquitinated protein aggregates and the autophagy machinery via dual binding domains, one for ubiquitin and one for LC3 [82, 83, 84] (Figure 1.2). This makes p62 degradation a reliable marker for autophagic flux [80].

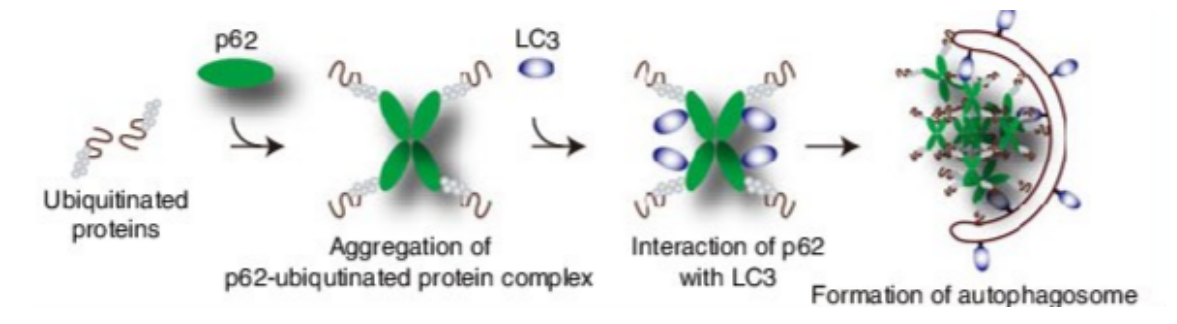


Figure 1.2: Selective autophagy mediated by p62 and LC3 interaction. p62/SQSTM1 acts as an autophagy receptor that recognizes ubiquitinated proteins through its UBA domain and simultaneously binds to LC3 via its LIR domain. This dual interaction facilitates the aggregation of p62-ubiquitinated protein complexes, which are then sequestered into the forming autophagosome through LC3-mediated membrane recruitment, ultimately leading to their degradation in the autolysosome. Figure adapted from Ichimura et al. [85].

1.2 Systems biology approach

Cellular information flows through different signaling pathways. As a signal traverses these pathways through a series of biochemical reactions and interactions, these processes cause dynamic changes in the concentrations of the various molecular species within

the network, allowing signal propagation to be observed through these concentration shifts [86]. These pathways can be considered as chemical reaction networks (CRNs), where each node of the network is one cellular species, and the edges between the nodes represent a biochemical reaction. Applying kinetic principles, such as mass action kinetics, allows the translation of a CRN into a system of Ordinary Differential Equations (ODEs), defining the rate constants and enabling the quantitative simulation of complex biochemical pathways [87]. The versatility of CRNs for quantitative chemical process modeling [88] is evident in its widespread application, for instance, in solid-state synthesis [89, 90], stable isotope fractionation prediction [91], electrochemistry [92, 93, 94], homogeneous and heterogeneous catalysis [95, 96, 97], and combustion kinetics [98].

However, a central challenge is that the rate constants and potentially other parameters governing these ODEs are often not well known, requiring the use of data-driven techniques such as parameter estimation or model calibration to approximate these values [99, 100, 101, 102, 103]. This process typically involves fitting the dynamic model (ODEs) to time-resolved experimental measurements of observable system outputs [104, 105]. Methodologically, this requires defining a quantitative objective function, frequently derived from statistical likelihood to properly account for measurement noise characteristics that measures the discrepancy between the model simulations generated with a given parameter set and the actual experimental data [106, 107]. Numerical optimization algorithms are then employed, usually involving multiple searches from different starting points or hybrid strategies, to identify the set of parameter values that minimizes this objective function, representing the best agreement between the model and the data [108, 109, 103]. Even with parameter estimation, the quality of the model can be compromised by noisy data, often from heterogeneous cell populations, which can introduce bias and overlook cell-to-cell variability [110, 103].

Achieving reliable model calibration faces significant challenges that must be carefully addressed [111, 103]. A fundamental challenge is parameter identifiability: parameters can be structurally non-identifiable if redundancies or symmetries in the model structure prevent their unique determination even with perfect data, or practically non-identifiable if the available experimental data lacks sufficient information content to constrain their values [112, 113, 114]. The optimization task is heavily dependent on the quality and informativeness of the experimental data, and these challenges, identifiability, optimization complexity, and data limitations tend to become more pronounced as the size and complexity of the biochemical network model increase [110]. Nevertheless, when both the structural properties of the network and the quality of the estimation are carefully considered through the workflow [115], these models have the potential to predict the dynamic behavior of complex biological systems with significant accuracy [116, 87]. To address

these challenges systematically, Villaverde et al. developed a comprehensive protocol that integrates structural identifiability analysis, parameter optimization, sensitivity analysis, and model validation into a unified framework (Figure 1.3), providing researchers with a robust methodology for ODE model calibration [103].

Model Calibration Process Input Optimal Experimental Design Mathematical model, parameters experimental data Inform experiment design 1. Structural Identifiability 2. Parameter Optimization 3. Sensitivity Analysis terative proces Objective function, estimation Most/least influential parameters Can parameters be uniquely determined? 4. Model Validation Output Goodness of Fit Calibrated Model Uncertainty Analysis

Figure 1.3: Workflow for calibrating and validating ordinary differential equation (ODE) models against experimental data. The process begins with input consisting of the mathematical model structure, initial parameter estimates, and experimental datasets. Optimal experimental design guides the collection of informative data to maximize parameter identifiability. The calibration workflow proceeds through four sequential steps: (1) Structural identifiability analysis to determine whether parameters can be uniquely determined from the available data, (2) Parameter optimization using objective function minimization in an iterative process, (3) Sensitivity analysis to identify the most and least influential parameters, and (4) Model validation through goodness-of-fit assessment and uncertainty analysis. The output is a fully calibrated and validated model ready for predictive applications [109].

Consequently, reliable parameter estimation in complex biochemical systems necessitates advanced software tools. Beyond merely solving the underlying ODE systems, such tools must adeptly integrate diverse direct and indirect experimental data, execute robust parameter optimization routines, and facilitate in-depth model analysis to ensure the credibility of the resulting models. Optima++ is a software framework that provides the capabilities needed to meet these requirements [117]. While its primary use case is in combustion chemistry, its design allows for broad application across chemical kinetics [117]. As biochemical pathways are fundamentally described as Chemical Reaction Networks (CRNs) and modelled using systems of Ordinary Differential Equations (ODEs), Optima++ is well suited for application to these biological systems. A key strength of Optima++ is it's FOCTOPUS global optimisation algorithm, which is specifically designed to robustly

optimise the rate parameters of kinetic models by simultaneously fitting them to multiple experimental data series from different sources [98]. For data handling and to ensure the reproducibility of optimisation studies, Optima++ uses the standardised "ReSpecTh Kinetic Data" (RKD) XML format [98, 118, 119]. These specific features, combined with the implementation of highly efficient CRN parameter identification algorithms, make Optima++ a powerful tool for addressing the quantitative complexity of biological networks and robustly estimating their many parameters.

1.3 In-silico models of autophagy

Numerous biochemical reaction network (BRN) models have been developed to capture complex cellular behaviors [120]. One of the most extensive in the literature is Liu et al.'s model, featuring over 94 species and 129 reactions. This model is structured around 5 major interconnected submodules: the Apoptosis module, the Autophagy module, the Calcium signaling module, the Inositol pathway module, and the mTOR signaling module (as summarized in Table 1.1). These modules collectively aim to represent and investigate the complex interplay between crucial cellular stress responses, particularly focusing on how cells integrate various signals to modulate processes like autophagy and apoptosis.

The parameters in Liu et al.'s original model were calibrated using image-based, single-cell experimental data obtained from Xu et al.'s study [121]. In these experiments, cells were exposed to various stress-inducing conditions, including staurosporine (STS), rapamycin, and tunicamycin (an ER stress-inducer that inhibits protein glycosylation), to observe the differential dynamics of cellular processes, with the data series primarily measuring cell death and autophagy levels [121]. While Liu et al. reported the estimated parameter values derived from this calibration, crucial details for exact replication, such as the specific initial concentrations for all 94 species and the precise sampling intervals used for their simulations, were not fully detailed in the original publication. The initial concentration of the species were defined randomly (presumably within plausible physiological bounds), then the average of multiple simulations subsequently considered to assess typical model behavior.

Table 1.1: Assessment of the five submodules in the autophagy-apoptosis computational model. \rightarrow denotes activation, \dashv denotes inhibition [120].

Submodule	Key Species	Effects on Autophagy/Apoptosis	Ref.
mTOR	mTORC1*,	mTORC1* ⊢ autophagy (blocks	[122,
	ULK1, AMPK,	ULK1, TFEB). AMPK \rightarrow au-	53]
	TFEB	tophagy (inhibits mTORC1*). No	
		direct apoptosis effects.	
Calcium	Ca ²⁺ (IC),	$Ca^{2+}(IC) \rightarrow autophagy$ (via	[123,
	CaMKK β ,	CaMKK β -AMPK). Ca ²⁺ (IC) \dashv	124]
	calpain	autophagy (via calpain cleavage).	
		$Ca^{2+}(IC) \rightarrow apoptosis$ (via calpain-	
		Bax).	
Inositol	cAMP, PLC ε^* ,	cAMP ⊢ autophagy (via EPAC-	[125]
	IP ₃	PLC ε^*). Indirectly $ o$ apoptosis (by	
		increasing Ca ²⁺).	
Autophagy	Beclin-1, Atg5,	Beclin-1, Atg5, UVRAG → au-	[126,
	UVRAG, Bcl-2	tophagy. Bcl-2 ⊢ autophagy. Cas-	127]
		pase cleavage of Beclin-1 ⊢ au-	
		tophagy, \rightarrow apoptosis.	
Apoptosis	p53, Bax, cas-	Nuclear p53 \rightarrow autophagy (DRAM).	[128,
	pase, PUMA	Cytoplasmic p53 ⊢ autophagy (in-	129]
		hibits AMPK). p53, Bax, PUMA \rightarrow	
		apoptosis. Caspase ⊢ autophagy.	

Although Liu's model is one of the most extensive, numerous other BCRN models in the literature investigate mechanisms relevant to its submodules. A common challenge in utilizing or adapting these published models lies in defining appropriate initial concentrations for their species, and the approaches vary. For instance, to simplify model optimization, some studies like Dalle et al. [130] and Bagci et al. [131] defined the initial concentrations of many species as zero, assigning non-zero values to only a select few. Other researchers, such as Sundaramurthy et al. [132], made assumptions based on protein function, positing higher concentrations for broadly regulating kinases compared to those with more limited specificity. Even when a source employs artificial units, as in the work by Tavassoly et al. [133], the underlying relationships can still be informative. In such cases, instead of relying on absolute values which may not be directly transferable, a strategy is to focus on the relative proportions of the species. This approach helps preserve the intended balance and stoichiometry between different proteins within the modeled system, allowing for meaningful comparative analysis even if the exact concentrations are

not directly applicable.

The intricate nature of molecular cellular processes such as the regulation of autophagy, with its extensive involvement in cellular homeostasis and numerous disease states such as neurodegenerative diseases and cancer [134, 135], presents a significant challenge that necessitates advanced quantitative methodologies [136]. While high-throughput technologies have greatly enhanced the ability to uncover system components and correlations, a deeper understanding of the underlying dynamic mechanisms is crucial for effective therapeutic intervention [137, 136]. The use of quantitative mechanistic models, such as Chemical Reaction Networks (CRNs), provides a robust framework to dissect the complex interplay of molecular interactions governing autophagy [137, 88]. These models allow for the simulation and analysis of dynamic behaviors, including feedback loops and control points within the autophagy pathway, which are often non-intuitive and difficult to predict solely from experimental data [137]. Such mechanistic insights are invaluable for translational medicine, offering the potential to identify novel drug targets and to simulate the effects of therapeutic interventions in silico [138, 139].

2 Objectives

My PhD research investigates ULK1-mediated autophagy induction using systems biology approaches to develop comprehensive models that enhance our understanding of these pathways. The work seeks to establish robust methodologies that enable direct applications in translational medicine. The specific objectives are:

1. To investigate the effect of the phosphatase PP2A on ULK1-mediated autophagy induction

- 1. Build a small-scale chemical reaction network (CRN) model incorporating PP2A and its connections to ULK1 and other relevant proteins.
- 2. Design experiments that generate time-series data for model optimization, and develop an effective parameter optimization strategy.
- 3. Analyze the dynamical characteristics of this network using the optimized model, with particular focus on feedback mechanisms and their contribution to robust and potentially periodic autophagy induction under various cellular conditions, including mTORC1 inhibition and PP2A modulation.

2. To determine the minimal dynamical requirements for ULK1-induced autophagy to oscillate

- 1. Address the discrepancy between our experimental observations, which reveal oscillatory dynamics in key autophagy proteins including ULK1, and our current computational models, which fail to reproduce these oscillations.
- 2. Identify and implement the minimal dynamical requirements needed for these models to reproduce oscillatory behavior.

3. To develop a more comprehensive, top-down modeling approach for autophagy regulation

1. Address the limitations of previous bottom-up modeling approaches (which focused on developing highly validated but limited-scope models of specific protein interactions) by adopting a top-down strategy.

- 2. Integrate previously developed small-scale models of autophagy regulation within a larger, more extensive biochemical reaction network framework, building upon published complex models such as that by Liu et al.
- 3. Develop and implement a robust, high-throughput numerical workflow capable of interpreting and integrating multiple data sources simultaneously from different experimental platforms.

3 Materials and methods

3.1 Experimental methods

This section describes the in vitro experimental methods used to examine autophagy. The experimental methods and materials described below were performed as previously published in our earlier works [51, 140, 54], and are presented here in detail for completeness.

3.1.1 Materials

Rapamycin (Sigma-Aldrich, St. Louis, MO, USA; R0395), okadaic acid (Sigma-Aldrich, 495604), Bafilomycin A1 (Sigma-Aldrich, M17931), DMEM—no glucose, no glutamine (Life Technologies, Carlsbad, CA, USA; A14430-01) were purchased. All other chemicals were of reagent grade.

3.1.2 Cell Culture and Maintenance

As model system, human embryonic kidney (HEK293T, ATCC, Manassas, VA, USA; CRL-3216) cell line was used. It was maintained in DMEM (Life Technologies, 41965039) medium supplemented with 10% fetal bovine serum (Life Technologies, 10500064) and 1% antibiotics/antimycotics (Life Technologies, 15240062). Culture dishes and cell treatment plates were kept in a humidified incubator at 37°C in 95% air and 5% CO_2 .

3.1.3 SDS-PAGE and Western Blot Analysis

Cells were harvested and lysed with 20 mM Tris, 135 mM NaCl, 10% glycerol, 1% NP40, pH 6.8. Protein content of cell lysates was measured using Pierce BCA Protein Assay (Thermo Scientific, Waltham, MA, USA; 23225). During each procedure equal amounts of protein were used. SDS-PAGE was done by using Hoefer miniVE (Amersham, UK). Proteins were transferred onto Millipore 0.45 µM PVDF membrane. Immunoblotting was performed using TBS Tween (0.1%), containing 5% non-fat dry milk (Sigma-Aldrich, 70166) or 1% bovine serum albumin (Sigma-Aldrich, A9647) for blocking membrane and

for antibody solutions. Loading was controlled by developing membranes for GAPDH in each experiment. For each experiment at least three independent measurements were carried out. The following antibodies were applied: antiLC3B (Santa Cruz Biotechnology, Dallas, TX, USA; sc-271625), antip62 (Cell Signaling Technology, Danvers, MA, USA; 5114S), antiULK1-Ser757-P (Cell Signaling Technology, 6888S), antiULK1 (Cell Signaling Technology, 8054S), antip70S6K-P (Cell Signaling Technology, 9234S), antip70S6K (Santa Cruz, sc-9202), antiAMPK-P (Cell Signaling Technology, 2531S), antiAMPK (Cell Signaling Technology, 2603S), antiPP2A-Tyr307-P (Sigma-Aldrich, SAB4503975), antiPP2A C Subunit (Cell Signaling Technology, 2259S) and antiGAPDH (Santa Cruz, 6C5), HRP conjugated secondary antibodies (Cell Signaling Technology, 7074S, 7076S). The bands were visualised using chemiluminescence detection kit (Thermo Scientific, 32106).

3.1.4 Silencing with siRNA

Cells were harvested and then seeded in six-well plates (200,000 cells/well) in antibiotic-free medium. Cells were allowed to settle overnight and transfected the next day. Lipofectamine RNAi Max (Invitrogen, Waltham, MA, USA; 13778075) reagent, GIBCOTMOpti-MEM I (GlutaMAXTM-I) reduced serum medium (Invitrogen, 31985070) and siRNA at a concentration of 20 pmol/ml were used for transfection. The ULK1 and PP2AC α siRNAs were purchased from Ambion (118259, 104510, s10957, s10958). The reagent was added to the cells and incubated for 24 h, followed by the treatments. Silencing efficiency was checked at protein levels.

3.1.5 Treatment with inhibitors

Table 3.1: Summary of treatments used in the studies

Substance	Concentration	Treatment	Effect	Pre-
		Time		treatment
Rapamycin	100 nM	2 hours	mTORC1 inhibition	No
akadaic acid	100 nM; 175	3 hours	PP2A inhibition	No
(OA)	nM			
Bafilomycin	100 nM	2 hours	Autophagic flux inhi-	Yes
A1			bition	
ULK1 silenc-	20 pmol/ml	24 hours	ULK1 downregula-	Yes
ing			tion	
PP2A silenc-	20 pmol/ml	24 hours	PP2A downregula-	Yes
ing			tion	
Rap + OA	100 nM each	2h (Rap) +	Combined mTORC1	No
		3h (OA)	and PP2A inhibition	

3.1.6 Statistics

For densitometry analysis Western blot data were acquired using ImageJ software. For the phosphorylated forms of p70S6K, ULK1, PP2A, and AMPK, relative band densities were normalized to the corresponding total protein, while LC3 II and p62 proteins' relative band densities were normalized to GAPDH. Then the treated data series were normalized for each protein with its own control. For each of the experiments three independent measurements were carried out. Results are presented as mean values \pm S.D. and were compared using t-Test (two sample assuming unequal variances) with Bonferroni correction (p-value correction). Asterisks indicate statistically significant difference from the appropriate control: ns—nonsignificant; *—p < 0.05; **—p < 0.01.

The quantitative analysis of the Western blot measurements was repeated with Azure-Spot Pro software to check the results acquired with ImageJ. The program contains 6 different background deduction method, we used the rolling ball method with a constant radius of 2 units. The different bands then were detected with the software's default setting, false detections were corrected by hand.

3.2 Computational methods

This section details the computational and mathematical modeling approaches employed in our publications that are discussed in this thesis [54, 141, 142].

3.2.1 Dynamical Systems Analysis

To investigate the qualitative dynamic properties of the constructed ODE models, including the existence and stability of steady states, bistability, and oscillatory behavior (limit cycles), standard dynamical systems analysis techniques were employed using the software package XPP-AUT [143].

Phase plane analysis was conducted on relevant two-dimensional systems or projections. This involved plotting nullclines for the state variables (curves where a variable's derivative is zero, e.g., $\frac{dX}{dt} = 0$) within the phase plane. Steady states (equilibrium points) were identified as the intersection points of these nullclines. The stability of these steady states (e.g., stable node/focus, unstable node/focus, saddle point) was determined by analyzing the eigenvalues of the system's Jacobian matrix evaluated at the equilibrium point, or inferred visually from the vector field and simulated system trajectories.

One-parameter bifurcation analysis was used to map how the system's steady states and/or periodic solutions (limit cycles) depend on key model parameters (bifurcation parameters). This involved using numerical continuation algorithms, typically accessed

via the AUTO package integrated within XPP-AUT, to track solution branches as the bifurcation parameter was varied quasi-statically. This process allowed for the detection of critical parameter values (bifurcation points) where the system's qualitative behavior changes, such as Hopf bifurcations (indicating the onset of oscillations) or saddle-node bifurcations (associated with switches between states or hysteresis).

The specific model equations, parameter values, choice of state variables for phase planes, and bifurcation parameters used for analyzing each distinct model are detailed in the relevant Methods subsections below and/or in the corresponding '.ode' implementation files available.

3.2.2 Computational Methods for PP2A-mTORC1-ULK1 Model

3.2.2.1 Mathematical Model Formulation

The model describes the interactions between mTORC1, ULK1, and PP2A, initially considering six state variables representing the active and inactive forms of each protein. The change in their concentrations over time was modelled assuming mass action kinetics for the underlying activation/inactivation reactions, resulting in a system of six ODEs. This system was reduced to three ODEs by applying conservation laws for the total amount of each protein ($mTOR_T, ULK1_T, PP2A_T$):

$$mTOR_T = mTOR_i + mTOR_a (3.1)$$

$$ULK1_T = ULK1_i + ULK1_a (3.2)$$

$$PP2A_T = PP2A_i + PP2A_a (3.3)$$

Substituting these conservation laws into the full system of ODEs yielded the following reduced system describing the dynamics of the active forms $(mTOR_a, ULK1_a, PP2A_a)$:

$$\frac{dmTOR_a}{dt} = k_{amtor} \cdot (mTOR_T - mTOR_a) - (k_{imtor} + k_{imtor1} \cdot ULK1_a + k_{imtor2} \cdot PP2A_a) \cdot mTOR_a$$
(3.4)

$$\frac{dULK1_a}{dt} = (k_{aulk} + k_{aulk1} \cdot PP2A_a) \cdot (ULK1_T - ULK1_a) - (k_{iulk} + k_{iulk2} \cdot mTOR_a) \cdot ULK1_a$$
(3.5)

$$\frac{dPP2A_a}{dt} = (k_{app2} + k_{app21} \cdot ULK1_a) \cdot (PP2A_T - PP2A_a) - (k_{ipp2} + k_{ipp21} \cdot mTOR_a) \cdot PP2A_a$$

$$(3.6)$$

The resulting model contains 12 unknown kinetic parameters $(k_{...})$ that require estimation from experimental data. The parameters of the model are available in the supplementary information of the original paper [54] and online at GitHub.

3.2.2.2 Structural Identifiability Analysis

Prior to parameter estimation for the PP2A-mTORC1-ULK1 model (Eqs. 3.4-3.6), a structural identifiability analysis was conducted to determine whether the 12 unknown kinetic parameters could, in principle, be uniquely determined from the model structure and planned measurements. This analysis was performed using the StructuralIdentifiability.jl package in Julia [144]. The analysis requires specifying the model outputs assumed to be measurable. In this case, the assessment was based on the assumption that measurements corresponding to both the active and inactive forms of mTORC1, ULK1, and PP2A could be obtained. This aligns with the experimental data collected (detailed in Section 3.1), where quantitative Western blot time-series measured phosphorylation levels indicative of activity (p70S6K-P for mTORC1, ULK1-Ser757-P, PP2A-Tyr307-P) as well as total protein levels for these components. From these measurements, the concentrations or relative activities of all six state variables (active and inactive forms) could be inferred, fulfilling the requirements for the identifiability assessment.

3.2.2.3 Parameter Estimation

The 12 unknown kinetic parameters of the PP2A-mTORC1-ULK1 model (Eqs. 3.4-3.6) were estimated by fitting model simulations to quantitative time-series data derived from Western blot experiments (see section 3.1 and Results Section 4.1). Specifically, data tracking protein phosphorylation states following short-term (1 hour) rapamycin or okadaic acid treatment in HEK293T cells were used [54].

Parameter estimation was formulated as an optimization problem aimed at minimizing a cost function, defined as the Mean Squared Error (MSE) between model predictions $(y_{s,j,k}^{sim}(p))$ and the corresponding experimental data points $(y_{s,j,k}^{exp})$:

$$MSE(p) = \frac{1}{N_{total}} \sum_{k \in Conds} \sum_{s \in Specs} \sum_{j \in Times_k} \left(y_{s,j,k}^{exp} - y_{s,j,k}^{sim}(p) \right)^2$$
(3.7)

Here, p represents the vector of kinetic parameters being estimated. The sums iterate over the experimental conditions used for fitting ($k \in \text{Conds}$, i.e., rapamycin and okadaic acid treatments), the measured species ($s \in \text{Specs}$, e.g., relative phosphorylation levels of p70S6K, ULK1, PP2A), and the measurement time points ($j \in \text{Times}_k$). N_{total} is the total number of experimental data points included in the sum.

The minimization was performed using the Limited-memory Broyden-Fletcher-Goldfarb-Shanno algorithm with bound constraints (L-BFGS-B) [145]. Key techniques employed during estimation included potentially using auxiliary functions (e.g., fitted cubic polynomials) to represent experimental data trends within the cost function, performing the optimization on logarithmic parameter scales ($\ln k$), and assigning fixed values to certain parameters representing assumed background activities based on biological reasoning [54].

3.2.2.4 Dynamical Systems Analysis

Dynamical analysis was performed using the XPP-AUT software following the methods described in subsection 3.2.1. This included phase plane analysis to investigate bistability (Figure 4.4) and bifurcation analysis to simulate different treatment conditions by varying total mTORC1 ($mTOR_T$) and PP2A ($PP2A_T$) concentrations. The specific reduced models and their corresponding '.ode' file implementations are available at GitHub.

3.2.2.5 Code Availability

The code implementing the PP2A-mTORC1-ULK1 model and analyses is available at https://github.com/eraut/pp2aMtorUlk [54].

3.2.3 Computational Methods for Autophagy Oscillation Model

3.2.3.1 Mathematical Model Formulation

To investigate the mechanisms underlying oscillatory dynamics in ULK1-dependent autophagy, particularly under cellular stress, an Ordinary Differential Equation (ODE) model was developed based on the core AMPK-mTORC1-ULK1 regulatory triangle [54]. Recognizing the potential need for time delays to generate oscillations [146], the model explicitly incorporates a hypothesized intermediary regulatory component ('REG') that mediates a delayed effect of AMPK.

The model tracks the dynamics of four variables representing the active forms or relative concentrations of ULK1, mTORC1 (denoted *mTOR*), AMPK, and REG. Interactions are described using first-order and Michaelis-Menten kinetics as defined in the following ODE system:

$$\frac{dULK1}{dt} = \frac{(k_{aulk} + k_{aulk1} \cdot REG + k_{aulk2} \cdot AMPK) \cdot (ULK1_T - ULK1)}{J_{ulk} + ULK1_T - ULK1} - \frac{(k_{iulk} + k_{iulk1} \cdot mTOR) \cdot ULK1}{J_{ulk} + ULK1}$$
(3.8)

$$\frac{dmTOR}{dt} = k_{amtor} \cdot (mTOR_T - mTOR) \tag{3.9}$$

$$-(k_{imtor} + k_{imtor1} \cdot AMPK + k_{imtor2} \cdot ULK1 + k_{imtor3} \cdot REG) \cdot mTOR$$

$$\frac{dAMPK}{dt} = \frac{(k_{aak} + STARV) \cdot (AMPK_T - AMPK)}{(J_{ampk} + AMPK_T - AMPK)} - \frac{(k_{iak} + k_{iak1} \cdot ULK1 + k_{iak2} \cdot mTOR) \cdot AMPK}{J_{ampk} + AMPK}$$
(3.10)

$$\frac{dREG}{dt} = \frac{(k_{areg} + k_{areg1} \cdot AMPK) \cdot (REG_T - REG)}{J_{reg} + REG_T - REG}$$

$$-\frac{k_{ireg} \cdot REG}{J_{reg} + REG}$$
(3.11)

Here, $ULK1_T$, $mTOR_T$, $AMPK_T$, and REG_T denote the total amounts or maximum activities. The STARV term represents the input stress signal. The 25 kinetic parameters $(k_{...}, J_{...})$ used were based on previous studies or estimations and are detailed in the original paper [141], and also available at Github.

3.2.3.2 Dynamical Systems Analysis

The dynamical behavior of this model, including its propensity for oscillations, was investigated through phase plane and bifurcation analyses using the methods described in Section 3.2.1 with the XPP-AUT software. Specific analyses involved varying the stress parameter (*S* or *STARV*) and examining projections like the ULK1-AMPK phase plane, using implementations defined in the relevant '.ode' files (e.g., 'full_bifurcaton.ode', 'mTOR_bifurcation.ode', 'ULK1_bifurcation.ode') available at GitHub.

3.2.3.3 Global Sensitivity Analysis (GSA)

To assess the impact of parameter uncertainty on model outputs like ULK1 levels, Global Sensitivity Analysis (GSA) was performed [147]. First-order (S_i) and total (S_{T_i}) Sobol indices were calculated using the variance-based eFAST method implemented in Julia

[148]:

$$Y = f(X_1, X_2, ..., X_n) (3.12)$$

$$S_i = \frac{Var_{X_i}(E_{X_{\sim i}}(Y|X_i))}{Var(Y)}$$
(3.13)

$$S_{T_i} = 1 - \frac{Var_{X_{\sim i}}(E_{X_i}(Y|X_{\sim i}))}{Var(Y)}$$
(3.14)

where Y is the model output, X_i are input parameters, and $X_{\sim i}$ denotes all parameters except X_i . For the analysis, parameter values were varied uniformly by $\pm 50\%$ around their nominal values.

3.2.3.4 Code Availability

The mathematical models and numerical analysis codes used for this study are available on GitHub (https://github.com/eraut/Autophagy_oscillation) [141]. Simulations and analyses were performed using XPP-AUT and potentially other tools as required. Protein levels/activities are given in arbitrary units (a.u).

3.2.4 Computational Methods for Basal State Model Calibration

The dynamics of the revised autophagy-apoptosis network model were described using a system of ODEs based on mass action kinetics, detailed in the wrok our previous work [142], reaction list also available at GitHub. Numerical simulations and parameter optimization were primarily performed using the Optima++ framework [118, 117], which interfaces with the CANTERA chemical kinetics solver [149] for ODE integration.

Optima++ minimizes a root-mean-square deviation (RMSD) type error function (E) to quantify the difference between simulation results and reference data (in this case, the target basal state ranges). Although originally developed for temperature-dependent combustion kinetics involving Arrhenius parameters $(k(T) = AT^n \exp(-E/RT))$, for these isothermal biological simulations, the rate coefficient was treated as a single temperature-independent value assigned to the pre-exponential factor A, with n and the activation energy $E_{Arrhenius}$ set to zero. Optimization was performed on the logarithm of the rate coefficients ($\ln A$) for efficient sampling across orders of magnitude.

3.2.4.1 Basal State Simulation and Error Quantification

To evaluate the model against the target basal state and for parameter optimization, 20 distinct initial condition sets ($N_{\rm cond} = 20$) were generated by uniform random sampling within physiologically plausible concentration ranges derived from literature (Supplementary Table S2). Each scenario was simulated for 24 hours. The deviation from the target

basal state was quantified using the following RMSD error function (E), calculated based on $N_{\rm spec} = 34$ selected indicator species whose basal ranges were well-defined:

$$E = \sqrt{\frac{1}{N_{\text{spec}} \cdot N_{\text{cond}} \cdot N_{\text{tim}}} \sum_{s=1}^{N_{\text{spec}}} \sum_{i=1}^{N_{\text{cond}}} \sum_{j=1}^{N_{\text{tim}}} \frac{(c_{s,i}^{\text{sim}}(t_j) - c_{s}^{\text{mean}})^2}{\sigma_s^2}}$$
(3.15)

Here, $c_{s,i}^{\text{sim}}(t_j)$ is the simulated concentration of species s at time point t_j (with $N_{\text{tim}} = 25$, representing hourly points) for condition i. c_s^{mean} is the center of the target basal range for species s, and σ_s represents one-eighth of the width of that range (i.e., the range is $[c_s^{\text{mean}} - 4\sigma_s; c_s^{\text{mean}} + 4\sigma_s]$). The species-specific error (E_s) was also calculated:

$$E_{s} = \sqrt{\frac{1}{N_{\text{cond}} \cdot N_{\text{tim}}} \sum_{i=1}^{N_{\text{cond}}} \sum_{j=1}^{N_{\text{tim}}} \frac{(c_{s,i}^{\text{sim}}(t_{j}) - c_{s}^{\text{mean}})^{2}}{\sigma_{s}^{2}}}$$
(3.16)

such that
$$E = \sqrt{\frac{1}{N_{\text{spec}}} \sum_{s=1}^{N_{\text{spec}}} E_s^2}$$
.

3.2.4.2 Sensitivity Analysis and Parameter Selection

To identify parameters most influential on the basal state, local sensitivity analysis was performed. The rate coefficient (k_n) of each of the 113 reactions was perturbed by +5% $(1.05 \cdot k_n)$, and the effect on simulations across all 20 conditions was computed. σ -normalized local sensitivity coefficients $(S_{s,i,n})$ were calculated via finite differences:

$$S_{s,i,n}(t_j) \approx \frac{1}{\sigma_s} \frac{c_{s,i}^{\text{sim}}(t_j; 1.05 \cdot k_n) - c_{s,i}^{\text{sim}}(t_j)}{\ln 1.05}$$
 (3.17)

An overall impact measure $(I_{n\to s}^{\text{SUE}})$, considering sensitivity (S), parameter uncertainty (U), and experimental error (E) as proposed by Kovács et al. [150], was used for ranking parameter influence:

$$I_{n \to s}^{\text{SUE}} = \sigma_n \cdot \sqrt{\frac{1}{N_{\text{cond}} \cdot N_{\text{tim}}} \sum_{i=1}^{N_{\text{cond}}} \sum_{j=1}^{N_{\text{tim}}} S_{s,i,n}^2(t_j)}$$
(3.18)

Here, σ_n relates to the parameter uncertainty. A uniform, large prior uncertainty corresponding to $f_n = 4$ (half-width of ± 4 orders of magnitude on a log10 scale, see [151]) was assumed for all reaction rate coefficients (k_n). Based on this analysis, 101 reactions were identified as influential and selected for optimization.

3.2.4.3 Parameter Optimization

Parameter optimization was performed using the FOCTOPUS algorithm within Optima++ [98]. FOCTOPUS (FOCusing robust Optimization with Uncertainty-based Sampling) employs iterative random or Gaussian sampling within defined uncertainty ranges, focusing the search around promising parameter sets and adjusting the sampling volume based on finding improvements, aiming for robust convergence. The objective was to minimize the overall RMSD error function (E, Eq. 3.15) by tuning the 101 influential rate coefficients within their ± 4 orders of magnitude uncertainty range. Due to parameters occasionally optimizing to the edge of this large range and becoming ineffective (too slow or too fast), the optimization involved multiple passes with manual intervention to reset specific parameters back to sensitive ranges before restarting optimization [142].

3.2.4.4 Posterior Uncertainty Analysis

The uncertainty of the final optimized parameters was estimated using the posterior covariance matrix method described by Turányi et al. [118], allowing quantification of the reduction in uncertainty achieved through the calibration process.

3.2.4.5 Software Implementation and Availability

The model simulations and analyses related to this basal state calibration were implemented primarily using the Optima++/CANTERA framework and supporting scripts in Julia and Python. The code implementing the revised and calibrated model is publicly available on GitHub (https://github.com/mcsksgyrk/basal_state_calibi, accessed on 10 September 2024) [142].

4 Results

4.1 Parameterization of a Core Autophagy Regulatory Model using Western Blot Time-Series Data

A minimal biochemical reaction network model focusing on the mTORC1, ULK1, and PP2A regulatory triangle was constructed and parameterized using experimental timeseries data generated by western blot [54]. These experiments involved quantitative measurements of the phosphorylation states of key network components over time following specific perturbations, providing the dynamic information necessary to constrain the kinetic parameters of the proposed regulatory network.

To describe the dynamic properties of the reaction network, the interactions between mTORC1, ULK1, and PP2A, shown schematically in Figure 4.1, were formulated as a system of ODEs assuming mass action kinetics for the underlying chemical reactions. The initial system considered six state variables, representing the concentrations of the active and inactive forms of each protein. By applying conservation laws for the total amounts of each protein (mTORC1, ULK1, PP2A), the number of ODEs was reduced to three. This minimal model structure contains 12 kinetic parameters whose values were estimated from experimental data.

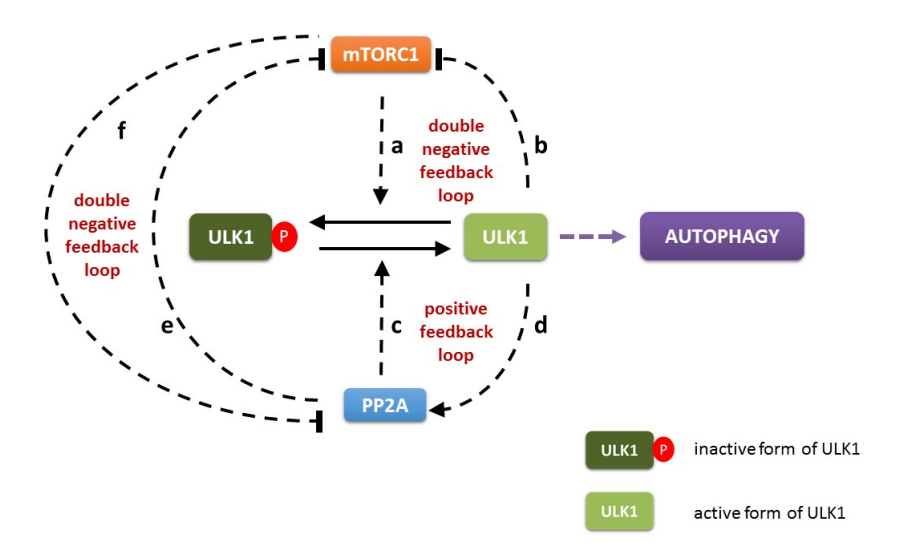


Figure 4.1: Wiring diagram of the core PP2A-mTORC1-ULK1 regulatory triangle model. Interactions include mutual inhibition between mTORC1-ULK1 (a, b) and mTORC1-PP2A (f, e), and positive feedback between ULK1-PP2A (d, c). Figure taken from our previous work [54].

Experimental time-series data were generated to characterize the dynamics of the mTORC1-ULK1-PP2A network following targeted perturbations shown in Supplementary Figure S1. Quantitative measurements tracked the phosphorylation states of p70S6K (mTORC1 activity), ULK1 (Ser757), and PP2A (Tyr307) after either mTORC1 inhibition with rapamycin (RAP) or PP2A inhibition with okadaic acid (OA). Inhibition of mTORC1 resulted in its rapid inactivation followed by subsequent activation of both ULK1 and PP2A (shown in Supplementary Figure S1 A, B). Conversely, inhibition of PP2A led to its sustained inhibition, resulting in mTORC1 hyper-activation and sustained ULK1 inhibition (shown in Supplementary Figure S1 D, E). This dataset formed the basis for parameterizing the mathematical model described previously.

Subsequently, the parameterized model was validated against experimental conditions that were distinct from those utilized for parameter fitting. This entailed the generation of new experimental data through the implementation of combined treatments in HEK293T cells, using chemical inhibitors and RNA interference (RNAi)-based gene knockdown methodologies. The experimental outcomes were utilized solely for the validation of the model, as it lacked prior knowledge.

Rapamycin was both combined with akadaic acid and PP2A siRNA, assuming their effect's magnitude differs. Inhibition via OA (resulting in functional inhibition indicated by PP2A hyper-phosphorylation) and siRNA knockdown (resulting in 25% residual PP2A protein), detailed in Figure 4.2 A, B. These distinct methods led to different outcomes for ULK1 activity: OA plus rapamycin allowed ULK1 activation, whereas siRNA knockdown plus rapamycin prevented ULK1 activation, as shown in Figure 4.2 A, B. The compu-

tational model, parameterized only on single-inhibitor data, successfully captured this differential response. Simulations predicted ULK1 activation under conditions mimicking OA plus rapamycin, shown in Figure 4.2 C, but predicted sustained ULK1 inactivity under conditions simulating siRNA knockdown, shown in Figure 4.2 D. The model's ability to reproduce these observed differential behavior under conditions not used for parameter estimation provided strong validation.

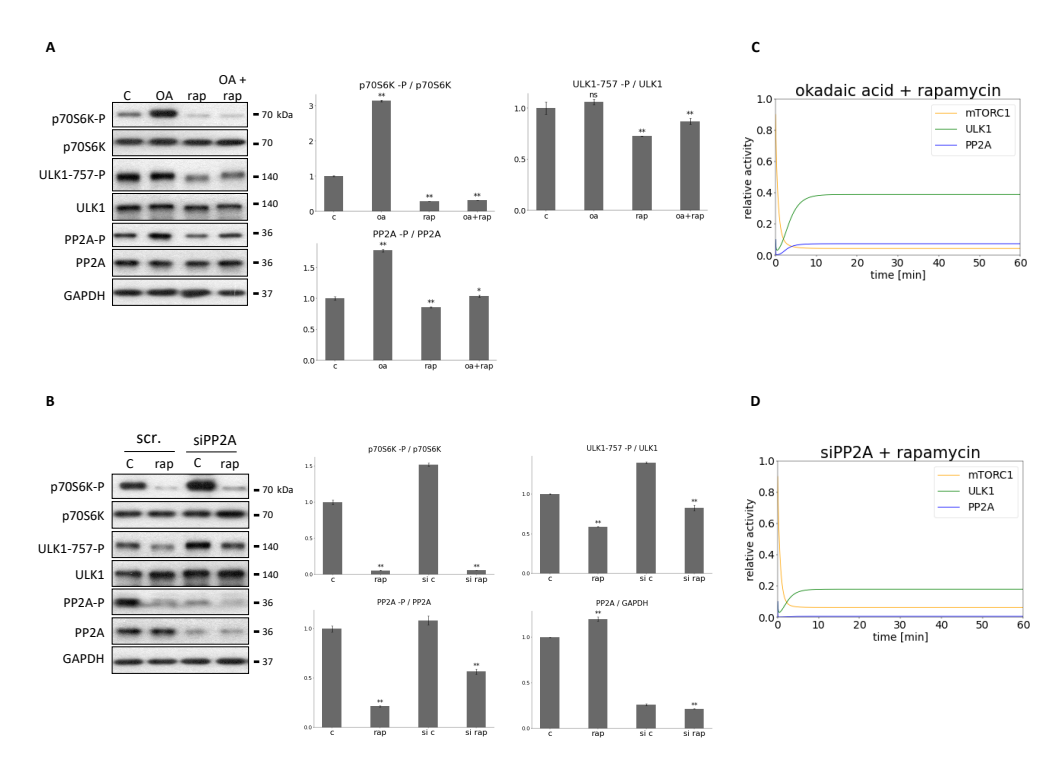


Figure 4.2: Combined down-regulation of both PP2A and mTORC1 can result in ULK1 activation. (A) HEK293T cells were treated with okadaic acid (OA), rapamycin (rap), or rap + OA (details in Methods). (B) PP2A was silenced (siPP2A) in HEK293T cells, then treated with/without rap (details in Methods). Scramble siRNA (scr.) used as control. (A,B, panel left) Immunoblots for indicated proteins. GAPDH as loading control. (A,B, panel right) Densitometry data (n=3). Error bars: SD; ns: non-significant; *p < 0.05; **p < 0.01 vs appropriate control. (C, D) Computational simulations of combined treatments mimicking OA+rap (C: PP2AT=0.1, mTORT=0.1) or siPP2A+rap (D: PP2AT=0.01, mTORT=0.1). Relative activities shown. Figure taken from our previous work [54].

Furthermore, the interplay involving ULK1 was investigated by combining ULK1 silencing with mTORC1 inhibition (rapamycin). Experimentally, under these conditions, PP2A remained largely inactive, as detailed in supplementary Figure S2 A, B. Computational simulations accurately predicted this outcome, showing minimal PP2A activation shown in Figure S2 C, D. This agreement between the model prediction and the experimental data for this independent condition provided additional validation for the model parameters and structure.

4.2 Oscillatory Dynamics in Autophagy Induction

Building on the observation of oscillations under mTORC1 inhibition [140], the question arose whether prolonged inhibition of the phosphatase PP2A could similarly result in periodic dynamics of the autophagy regulatory network. To investigate this, and for comparison with known oscillatory behavior, HEK293T cells were treated over time courses with either 100 nM OA for 180 min or 100 nM rapamycin for 120 min (Figure 4.3). For both treatments shown, key indicators including mTORC1 activity (p70S6K phosphorylation), ULK1 status (Ser-757 phosphorylation), PP2A status (Tyr307 phosphorylation), and autophagy markers (LC3II/I ratio, p62 levels) were monitored via immunoblotting (Figure 4.3A, B). Additionally, for the rapamycin treatment, AMPK phosphorylation status was tracked, reproducing the previously reported oscillatory dynamics involving these core components (Figure 4.3B, D) [140]. Focusing on the 100 nM OA treatment (Figure 4.3A, C), the activation state of the monitored regulatory proteins displayed a pronounced rhythmic pattern, with an approximate period of 1.5 hours. The phosphorylation profiles of p70S6K, ULK1, and PP2A oscillated over the time course. Notably, the apparent activation of ULK1 and PP2A (indicated by decreased phosphorylation) coincided with decreased p62 levels and increased LC3II/LC3I ratios, suggesting periodic induction of autophagy. Conversely, mTORC1 activity peaked when ULK1 and PP2A appeared less active. These experiments were conducted using non-synchronized cell populations to minimize potential confounding effects from the cell cycle or circadian rhythms.

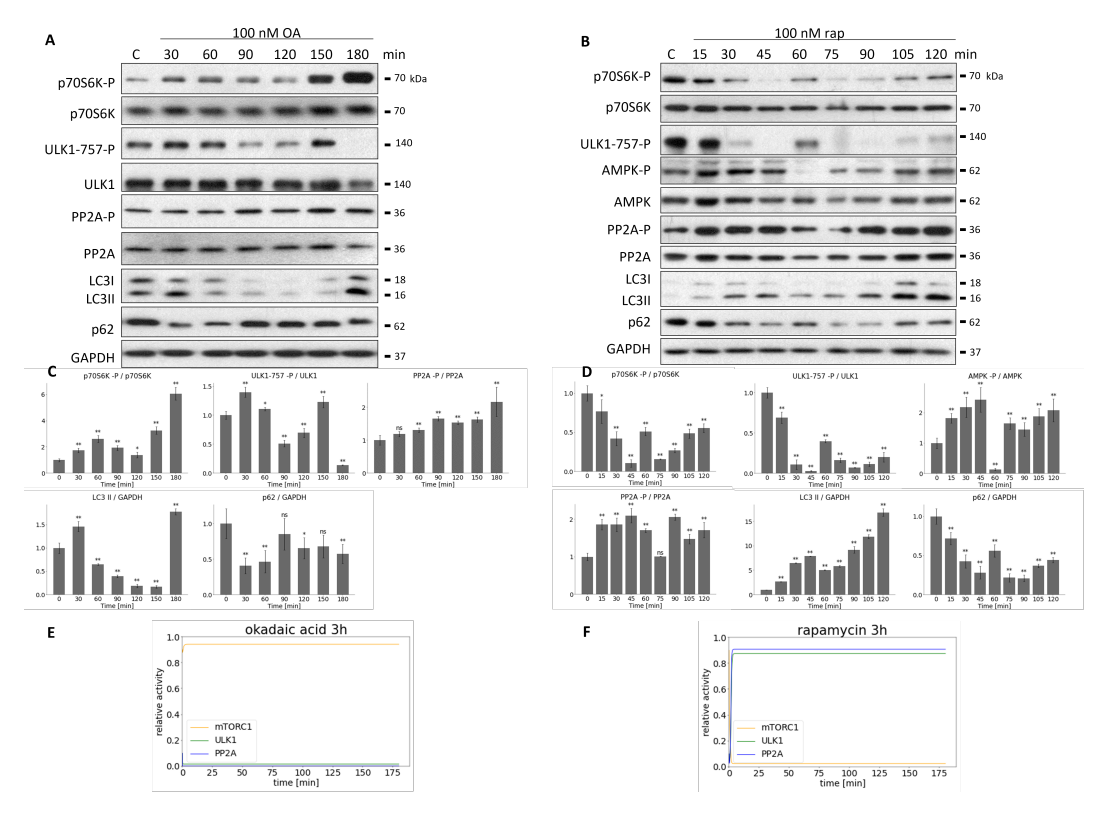


Figure 4.3: Prolonged OA or rapamycin treatment results in distinct oscillatory dynamics of autophagy-related proteins. HEK293T cells were treated over time with either (A) 100 nM okadaic acid (OA) for 180 min or (B) 100 nM rapamycin (rap) for 120 min. Markers for mTORC1 activity (p70S6K-P), ULK1 phosphorylation (ULK1-757-P), AMPK phosphorylation (AMPK-P, *rapamycin panel only*), PP2A phosphorylation (PP2A-P), and autophagy (LC3I/II, p62) were assessed by immunoblotting. GAPDH was used as a loading control. (C, D) Densitometry data corresponding to panels A and B, respectively. Intensities of phosphorylated proteins (p70S6K-P, ULK1-757-P, AMPK-P, PP2A-P) were normalized to their respective total protein levels (where applicable, total levels shown in A/B) or GAPDH. LC3II and p62 intensities were normalized to GAPDH. Data represent mean \pm SD (n=3). Asterisks indicate statistically significant difference from the control (C, time 0): ** p < 0.01, * p < 0.05. (E, F) Corresponding computational simulations showing relative activities under simulated OA or rapamycin treatment over 3 hours, based on the model from [54].

Interestingly, in case of prolonged treatment with even higher level of OA (175 nM for 180 min) no periodic repeat of either mTORC1 or ULK1 was observed (Figure 4.3 B), suggesting that this above mentioned characteristic feature of the control network was highly dependent on the level of PP2A inhibition. To further confirm that autophagy induction has been properly achieved, the above mentioned OA treatments were combined with a well-known autophagy inhibitor, called Bafilomycin A1 (supplementary Figure S4). When autophagy flux was inhibited, higher levels of LC3II/GAPDH and p62/GAPDH were obtained, confirming that autophagy functioned properly during pure OA treatment

4.2.1 Characteristic of Autophagy Induction

The experimental results demonstrated complex dynamics, including oscillations under specific OA concentrations. To explore the fundamental dynamical properties embedded within the core mTORC1-ULK1-PP2A model structure that might explain such behaviors or potential discrepancies under different conditions, phase plane analysis was employed. This analysis investigates the model's steady-state landscape by examining the intersections of the nullclines (balance curves) for ULK1 and mTORC1 activity (Figure 4.4).

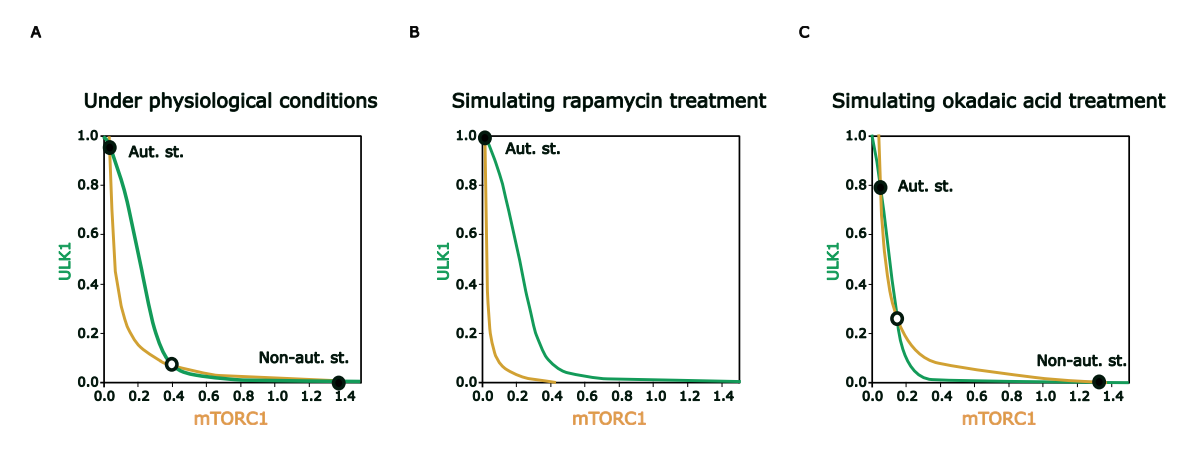


Figure 4.4: The dynamical feature of PP2A-mTORC1-ULK1 regulatory triangle controlled stress response mechanism. Phase plane diagram of PP2A-mTORC1-ULK1 regulatory triangle (**A**) under physiological conditions, upon (**B**) rapamycin (mTORT = 0.1) or (**C**) OA treatment (PP2AT = 0.3). The balance curves of ULK1 (green curve) and mTORC1 (orange curve) are plotted. Stable and unstable steady states are visualized with black and white dots, respectively. "Non-aut. state" refers to non-autophagy state (with active mTORC1 and inactive ULK1), while "Aut.st." refers to "autophagy state" (with active ULK1 and inactive mTORC1) [54].

The intersections of these nullclines indicate the system's equilibrium points. Due to the interplay of the positive feedback loop (ULK1 \rightarrow PP2A \rightarrow ULK1) and the two double-negative feedback loops (mTORC1 \dashv ULK1; ULK1 \dashv mTORC1; mTORC1 \dashv PP2A; PP2A \dashv mTORC1), the nullclines intersect at three points under simulated physiological conditions (Figure 4.4 A). Two of these intersections represent stable steady states, separated by an unstable one. These stable states correspond to distinct cellular conditions: a "Non-autophagy state" with high mTORC1 activity and low ULK1 activity, and an "Autophagy state" characterized by low mTORC1 and high ULK1 activity. Under normal conditions, the system resides in the "Non-autophagy state".

This bistable structure allows the system to function as a switch in response to strong perturbations. Simulating mTORC1 inhibition (akin to rapamycin treatment) shifts the

mTORC1 nullcline leftward, effectively removing the "Non-autophagy" stable state (Figure 4.4B). This forces the system into a decisive transition towards the sole remaining stable equilibrium, the "Autophagy state". Conversely, simulating PP2A inhibition (akin to OA treatment) preserves both stable states (Figure 4.4C); since the system originates with high mTORC1 activity, it remains in the "Non-autophagy state" despite the perturbation. While demonstrating the system's capacity for decisive state changes, this switch-like behavior between stable states does not, by itself, explain the sustained periodic oscillations observed experimentally (subsection 4.2.3).

Therefore, this phase plane analysis confirms the core regulatory triangle's inherent capacity for bistable switching, enabling robust transitions between distinct cellular states based on stimulus type and strength. However, this bistable characteristic alone is insufficient to account for sustained oscillatory dynamics.

4.2.2 Requirement for Model Refinement to Explain Sustained Oscillations in the AMPK-mTORC1-ULK1 Network

Although the PP2A-mTORC1-ULK1 core network exhibits bi-directionality (subsection 4.2.1), this feature alone does not account for the sustained oscillations observed experimentally under certain conditions (subsection 4.2.3). To delve deeper into the mechanisms required for such periodic behavior, focus shifted to the AMPK-mTORC1-ULK1 regulatory triangle. This network shares a similar size and feedback structure to the PP2A-containing model previously discussed. The capacity of this specific AMPK-mTORC1-ULK1 network to generate robust limit cycle oscillations upon relevant stimuli like nutrient stress or rapamycin treatment has been previously demonstrated and experimentally validated by our group [140].

Given that the fundamental oscillatory characteristic of the AMPK-centric network was well-established, the subsequent investigation presented in [141] utilized this framework to explore the precise mechanistic requirements needed to ensure the model robustly captures these nuanced dynamics. Initial analysis revealed that simplified representations of the direct feedback loops within this validated AMPK-mTORC1-ULK1 network were insufficient to consistently reproduce oscillations across all conditions. Specifically, simulations incorporating the direct AMPK \dashv ULK1 negative feedback and the AMPK \dashv mTORC1 double-negative feedback loop, while capable of producing oscillations under simulated stress, failed to do so under simulated rapamycin treatment (Figure 4.5). As shown in Figure 4.5B (lower panel), this model predicted a collapse to a stable steady state, contradicting experimental findings.

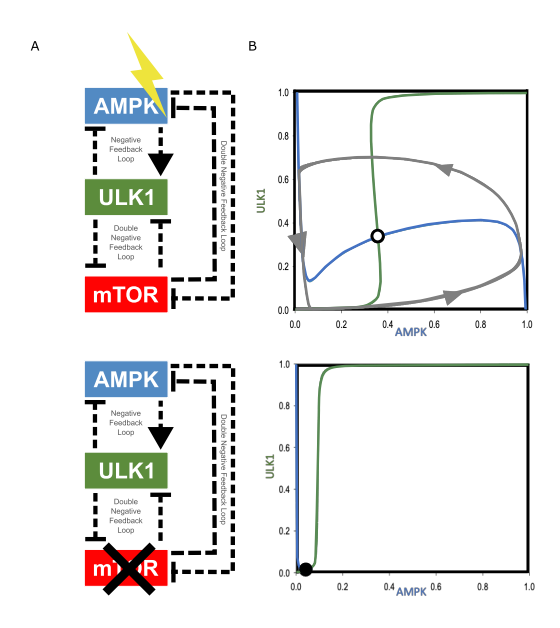


Figure 4.5: Dynamics of the core ULK1-mTOR-AMPK regulatory triangle. (A) Wiring diagram of the ULK1-AMPK-mTOR regulatory network under cellular stress (upper panel, stress = 3) or rapamycin treatment (lower panel, mTORT = 0.01). Dashed lines indicate regulatory interactions; blocked-end lines denote inhibition. (B) Phase plane analysis showing nullclines for ULK1 (green) and mTOR (red) under cellular stress (upper) or rapamycin treatment (lower). Filled and unfilled circles mark stable and unstable steady states, respectively, at nullcline intersections; grey dotted lines show system trajectories. Throughout this figure, mTOR refers to mTORC1. Adapted from [141].

4.2.3 A Time-Delayed Negative Feedback Model Reproduces Oscillations

Simulations indicated that incorporating a time delay was sufficient to enable limit cycle oscillations within the model system. Therefore, a time delay was introduced to the system. There are two options for this as discussed by Holczer et al. [140]: either through multiphosphorylation, or through an intermediary protein. We implemented the second option by constructing a model featuring a regulatory protein ('REG') activated by AMPK, which subsequently promotes ULK1 activity while inhibiting mTORC1 (Figure 4.6). This REG component mediates a delayed effect of AMPK through the negative feedback loop influencing ULK1 (AMPK \rightarrow REG \rightarrow ULK1 \dashv AMPK). Computational simulations of this extended model demonstrated that this structure, incorporating the delayed negative feedback and REG-mediated mTORC1 inhibition, successfully generated sustained limit cycle oscillations (Figure 4.6). These oscillations were robust under conditions mimicking both cellular stress and direct mTORC1 inhibition (rapamycin), aligning with experimental observations. Furthermore, global sensitivity analysis (GSA) using the Sobol method indicated the structural importance of this delayed feedback. The results of the GSA

suggested that the model output (e.g., ULK1 levels, indicative of oscillatory behavior) was most dependent on the input stress levels and the strength of the ULK1 \dashv AMPK interaction [141]. The parameter governing the AMPK \rightarrow REG reaction also ranked highly (fourth highest Sobol index for ULK1 level), confirming the significant impact of this reaction, central to the delay mechanism, on the overall system dynamics, even with loosely defined parameter values (see Supplementary Figure S5).

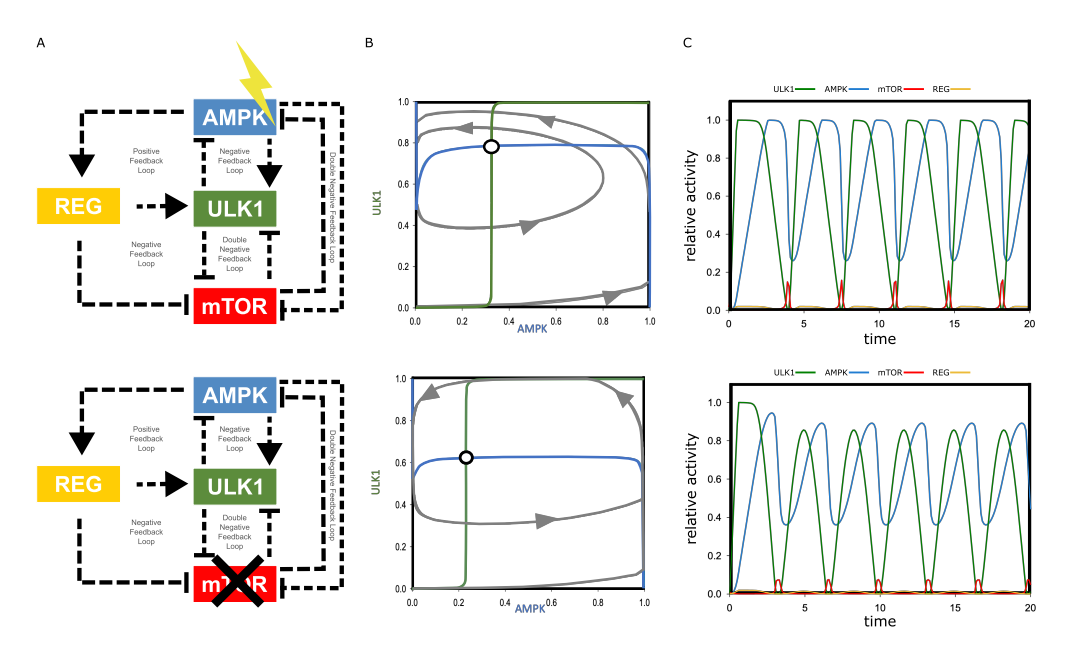


Figure 4.6: Time-delayed dynamics of the ULK1-mTOR-AMPK regulatory triangle with an additional regulatory protein. (A) Wiring diagram of autophagy induction under cellular stress (upper panel, stress = 0.5) or rapamycin treatment (lower panel, mTORT = 0.5). Dashed lines indicate regulatory interactions; blocked-end lines denote inhibition. (B) Phase plane analysis showing nullclines for ULK1 (green) and AMPK (blue) under cellular stress (upper) or rapamycin treatment (lower). Unfilled circles mark unstable steady states at nullcline intersections; grey dotted lines show system trajectories. (C) Temporal dynamics of mTOR, AMPK, ULK1, and REG relative activities under cellular stress (upper) or rapamycin treatment (lower). Throughout this figure, mTOR refers to mTORC1. Adapted from [141].

4.2.4 The Delay Mechanism via REG is Essential for Oscillatory Dynamics

To confirm the necessity of this intermediary component and the delay it introduces, further simulations were performed where the functional connections involving REG were disrupted. Specifically, eliminating the positive effect of REG on ULK1 (REG \rightarrow ULK1) resulted in a failure to activate ULK1 and induce autophagy, despite AMPK activation and mTORC1 inhibition (Figure 4.7 A). Similarly, removing the inhibitory effect of REG on mTORC1 (REG \dashv mTORC1) prevented the necessary downregulation of mTORC1,

keeping both ULK1 and AMPK inactive and blocking autophagy induction (Figure 4.7B). These results underscore that both regulatory actions of the proposed REG component are essential for the model to exhibit the correct dynamic behavior, including oscillations and proper autophagy activation upon stress.

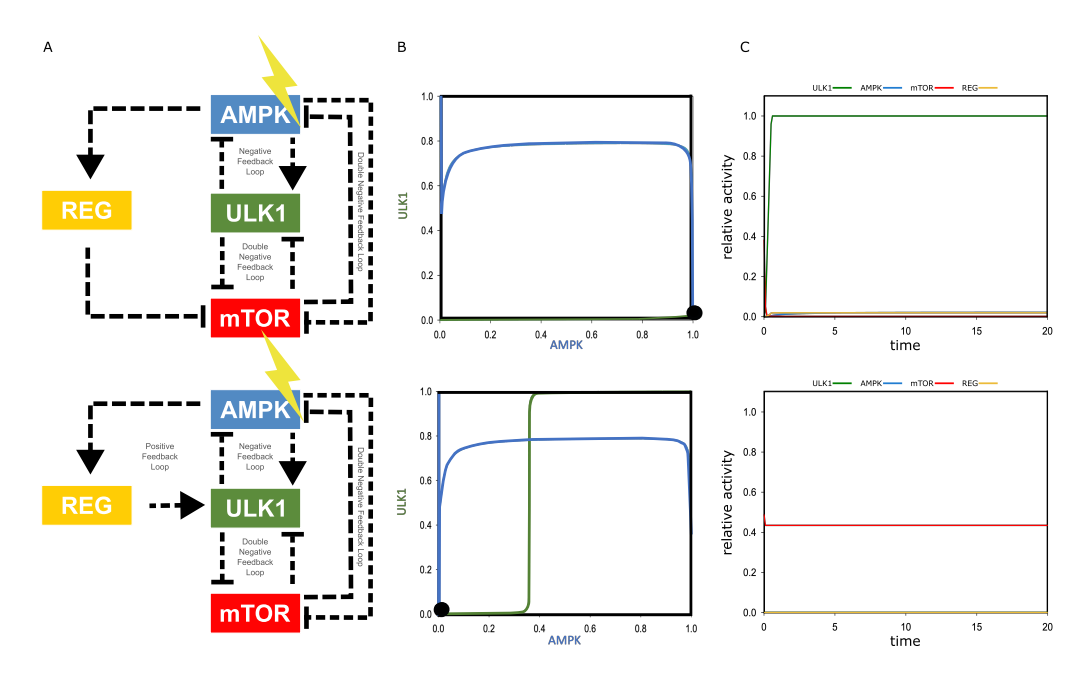


Figure 4.7: Essential role of the regulatory protein (REG) in autophagy induction under cellular stress. (A) Wiring diagram showing the effects of removing specific REG interactions: $REG \rightarrow ULK1$ activation (upper panel, $k'_{aulk} = 0$) or $REG \dashv mTOR$ inhibition (lower panel, $k'''_{imtor} = 0$). Dashed lines indicate regulatory interactions; blocked-end lines denote inhibition. (B) Phase plane analysis showing nullclines for ULK1 (green) and mTOR (red) when $REG \rightarrow ULK1$ (upper) or $REG \dashv mTOR$ (lower) connections are removed. Filled and unfilled circles mark stable and unstable steady states, respectively, at nullcline intersections; grey dotted lines show system trajectories. (C) Temporal dynamics of mTOR, AMPK, ULK1, and REG relative activities when $REG \rightarrow ULK1$ (upper) or $REG \dashv mTOR$ (lower) connections are removed. All simulations performed under cellular stress conditions. Throughout this figure, mTOR refers to mTORC1. Adapted from [141].

4.3 Autophagy-Apoptosis Model calibration, a Top-Down approach

The core autophagy regulatory network studied previously provides limited insight into the broader cellular context of autophagy regulation. To address this limitation, we adopted the comprehensive chemical reaction network model published by Liu et al. [120] as a foundational framework for systems-level analysis [142]. However, the reproducibility of this model was hindered by the absence of publicly available source code and

essential simulation details, particularly initial species concentrations [142]. Moreover, simulations employing a reconstruction based on published information demonstrated an inability to maintain a stable basal state, exhibiting inappropriate pathway activation [142]. Consequently, substantial revisions to the reaction network topology and extensive parameter recalibration were required to establish a reliable, reproducible, and physiologically relevant basal state model, as detailed in the subsequent sections.

4.3.1 Defining the initial concentrations

Defining appropriate initial concentrations for the 84 model species was necessitated by the lack of such data in the original Liu et al. publication [120]. Plausible physiological ranges were therefore established via a literature review of comparable quantitative models (summarized in our [142]), acknowledging the general sparsity of absolute protein concentration data [142]. The target basal state was assumed to be proliferating, characterized by active mTORC1 signaling, low constitutive autophagy, inactive apoptosis, and standard cytoplasmic (~ 100 nM) and ER ($\sim \mu$ M) calcium levels. A standard cell volume (10^{-12} L) ensured unit consistency, and species lacking specific literature data were assigned a generic 0-100 nM range. The resulting initial concentration ranges used for simulation are shown in Supplementary Table S2.

4.3.2 Revision of Incorrect Reactions

Analysis of the reconstructed Liu et al. model identified several inconsistencies with known biology, necessitating targeted modifications to achieve a realistic basal state simulation [142]. The key revisions implemented were:

- Stress pathway removal: Complex ER stress signaling pathways involving PERK and JNK were excluded to enable focused calibration of the metabolic basal state without stress-induced perturbations.
- PKA mechanism correction: PKA's role was corrected from autophagy promotion
 to inhibition, aligning with experimental evidence on LC3 regulation. The activation
 mechanism was updated to be cAMP-dependent rather than MAPK15-dependent,
 with MAPK15 removed entirely from the model.
- PKC role reversal and feedback addition: PKC's function was corrected from autophagy promotion to inhibition, and a new feedback loop was introduced whereby PKC regulates cAMP signaling through PLC modulation.

- mTOR-ULK1 interaction refinement: The interaction mechanism was changed from complex formation to direct phosphorylation, better reflecting the established inhibitory phosphorylation of ULK1 by mTORC1.
- **AKT-mTORC1 pathway correction:** The erroneous reaction mTOR_ULK + AKTA → mTOR + ULKA + AKTA, which incorrectly suggested AKT inhibits mTORC1, was removed. This corrects the directionality to reflect AKT's established role in activating mTORC1.

These modifications resulted in a revised network model comprising 113 reactions and 84 species shown in Figure 4.8, which formed the basis for subsequent parameter optimization [142]. The reactions of the model are shown in Supplementary Figure 10.

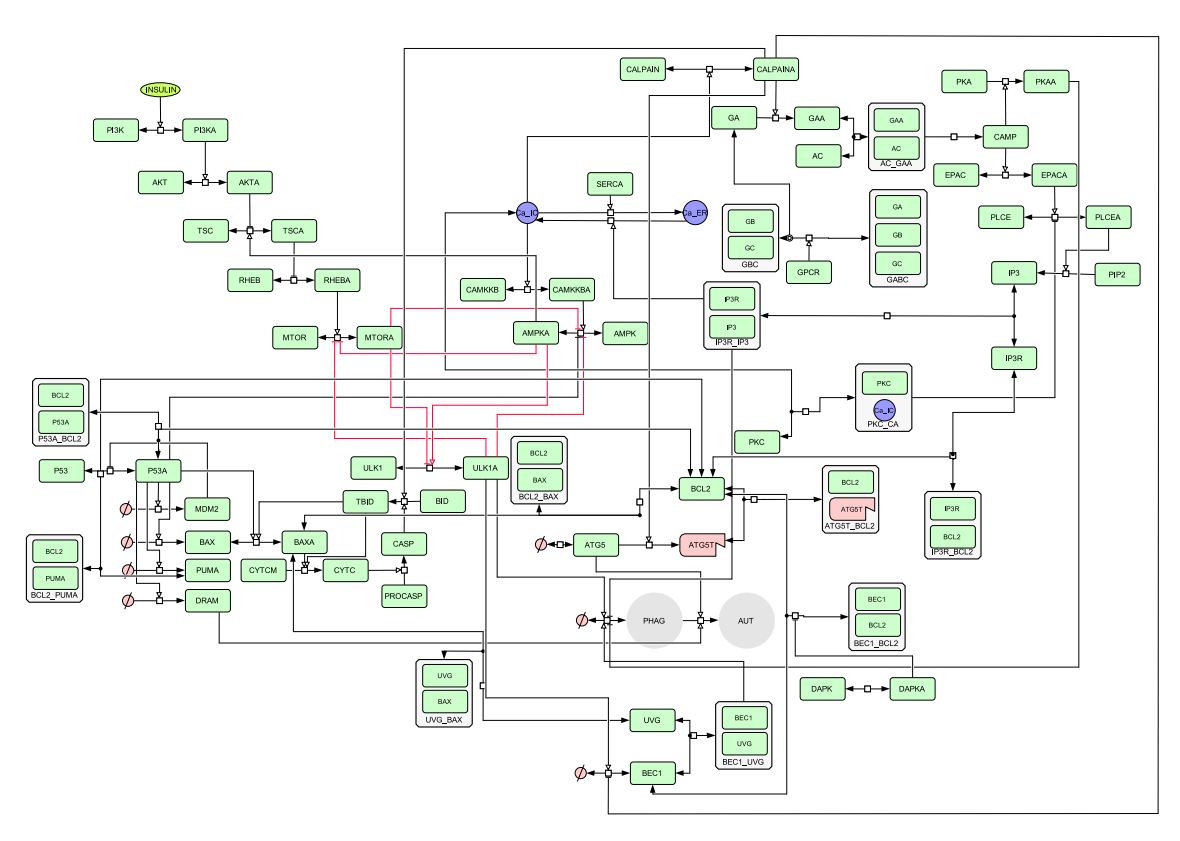


Figure 4.8: Wiring diagram of the enhanced autophagy-apoptosis signaling network model. This comprehensive network integrates key regulatory modifications described in the main text (including refined PKA/PKC/AKT signaling roles and streamlined stress response pathways) into the original Liu et al. framework [120], resulting in a model of 113 reactions and 84 molecular species used for basal state calibration [142]. Critical regulatory connections within the AMPK-mTOR-ULK1 control hub are emphasized with red connection lines. The complete mathematical formulation of all reactions, parameter values, and kinetic equations are provided in Supplementary Figure 10, which presents the full reaction network in detail for computational implementation and analysis.

4.3.3 Identification and Optimization of Influential Rate Coefficients

To calibrate the revised model, influential parameters were first identified using local sensitivity analysis (detailed in subsection 3.2.4 or in [142]). This analysis determined that 101 out of 113 reaction rate coefficients significantly impacted the simulated basal state dynamics [142].

Subsequently, these 101 influential parameters were optimized using the Optima++ code with the FOCTOPUS algorithm [142]. The optimization aimed to minimize the overall RMSD error (E) between simulations across 20 initial conditions and the target basal state, tuning parameters within a ± 4 orders of magnitude uncertainty range. The iterative process successfully reduced the overall error E substantially, from an initial value of approximately 1.3×10^9 down to a final value of 2.22. Species-specific errors (E_s) were also dramatically reduced; for instance, the error for the critical apoptosis regulator BAX decreased from 2.1×10^{10} to 3.37 (Table 4.1).

Table 4.1: Comparison of species-specific root-mean-square errors (one-day simulations of 20 conditions) of the concentration-time profiles simulated with the initial and final optimized mechanisms, sorted from highest (red) to lowest (green). Species are referred to by their name in the model [142].

Species	ini	opt	Species	ini	opt
BAX	2.09×10^{10}	3.37	CAMKKB	2.72	2.24
BCL2_BAX	39.0	2.24	DAPK	2.63	2.63
UVG	7.85	2.39	PROCASP	2.38	2.56
BCL2	7.85	1.81	PIP2	2.46	2.32
BCL2_PUMA	7.83	2.26	AC	2.35	2.36
AKTA	7.71	2.20	CALPAIN	2.36	2.23
BEC1	7.22	2.27	GPCRA	2.34	2.34
ATG5T	7.01	1.67	GA	1.99	2.28
RHEBA	6.63	2.08	PKA	2.25	2.26
CA2IC	6.40	2.09	P53	2.24	2.24
ATG5	5.93	1.14	CA2ER	2.22	2.12
TSC	5.68	2.06	GBC	2.20	2.13
MTORA	5.44	2.60	SERCA	2.18	2.18
ULK	4.21	1.92	AMPK	2.17	2.12
IP3	4.06	2.28	CYTCM	2.05	2.03
BID	3.61	1.74	EPAC	1.84	1.84
PKC	3.21	2.53	PLCE	1.80	1.80

The resulting calibrated model accurately simulates stable homeostasis, maintaining key species concentrations like MTORA, ULK, PROCASP, and CA2ER within their physiological basal ranges over 24 hours, which stands in clear contrast to the initial model's

failure (Figure 4.9). Furthermore, the calibration significantly constrained the uncertainties of many rate coefficients. Posterior analysis revealed that parameter uncertainties were reduced to within one order of magnitude for 19 reactions, within two orders of magnitude for 72 reactions, within three for 6 reactions, and between four and five for 1 reaction (Table 4.2; [142]).

Table 4.2: Prior and posterior rate coefficient values and uncertainty ranges for reactions with the most constrained rate coefficients in ascending order (green lowest, yellow highest). The rate coefficients values for the reactions are taken in $\frac{1}{s}$ and $\frac{cm^3}{mol \cdot s}$ units, respectively [142].

#	Reaction	log ₁₀ k _{ini}	f_{prior}	log ₁₀ k _{opt}	f _{posterior}	$10^{f_{posterior}}$
73	ATG5T+BCL2→ATG5_BCL2	6.50	4.00	4.79	0.13	1.35
43	IP3→PIP2	-3.55	4.00	-5.15	0.14	1.37
104	ATG5→REF	-4.55	4.00	-4.51	0.19	1.55
102	REF→ATG5	-15.55	4.00	-14.23	0.20	1.57
109	PKC+CA2IC→PKC_CA2IC	5.44	4.00	4.17	0.26	1.81
10	$BCL2_BAX \rightarrow BCL2 + BAX$	-3.50	4.00	-5.76	0.26	1.84
63	$MTORA \rightarrow MTOR$	-3.55	4.00	-3.45	0.60	3.98
71	$AKTA \rightarrow AKT$	-3.53	4.00	-6.30	0.63	4.25
54	EPACA→EPAC	-3.50	4.00	-4.83	0.63	4.26
18	$REF \rightarrow BID$	-17.59	4.00	-16.63	0.65	4.49
30	$PUMA \rightarrow REF$	-3.92	4.00	-4.99	0.73	5.36
29	$BCL2_PUMA \rightarrow PUMA + BCL2$	-3.08	4.00	-3.34	0.87	7.36
69	RHEBA+MTOR \rightarrow RHEBA+MTORA	6.45	4.00	8.16	0.88	7.65
28	$PUMA+BCL2{\rightarrow}BCL2_PUMA$	7.22	4.00	7.91	0.89	7.70
9	$BCL2+BAX \rightarrow BCL2_BAX$	6.54	4.00	3.18	0.94	8.77
8	P53A_BCL2→P53A+BCL2	-6.78	4.00	-6.32	0.97	9.32
44	CA2IC+CAMKKB→CA2IC+CAMKKBA	5.44	4.00	3.12	0.99	9.73
34	CA2IC+SERCA→CA2ER+SERCA	7.01	4.00	3.47	1.00	10.00
45	$K\text{+}CAMKKBA {\rightarrow} AMPKA\text{+}CAMKKBA$	6.44	4.00	6.05	1.00	10.00

4.3.4 Optimized Model Validation and Parameter Constraints

The 20 concentration vs. time curves $(c_{s,i}^{\text{sim}}(t_j), j = 0...24)$ for four key species—active mTOR (MTORA), inactive ULK (ULK), procaspase (PROCASP), and $\text{Ca}_{\text{ER}}^{2+}$ (CA2ER)—illustrate the performance of the calibrated model (Figure 4.9). These species were selected for their critical roles in signaling cell growth (MTORA), autophagy activity (ULK), apoptosis (PROCASP), and calcium homeostasis (CA2ER), which influences both autophagy and apoptosis. The simulations clearly show that while the initial model (red lines) predicted physiologically incorrect dynamics like mTOR inactivation and procaspase consumption, the optimized mechanism (green lines) successfully sustains the concentrations of these key markers within their expected basal physiological ranges over 24 hours. Concentration profiles for all 34 monitored species are available in the supplementary information associated with [142].

The optimization process significantly constrained the uncertainty of many kinetic parameters, leveraging the requirement to accurately simulate the basal state. Posterior uncertainty analysis, using methods described by Turányi et al. [118], quantified this refinement. Table 4.2 summarizes the results for the 19 reactions whose rate coefficients were most constrained, achieving uncertainty bounds within one order of magnitude $(10^{f^{\text{posterior}}} < 10)$. As detailed in our previous work, the optimization constrained the rate coefficients of 19, 72, 6, and 1 reactions within 0–1, 1–2, 2–3, and 4–5 orders of magnitude uncertainty, respectively [142].

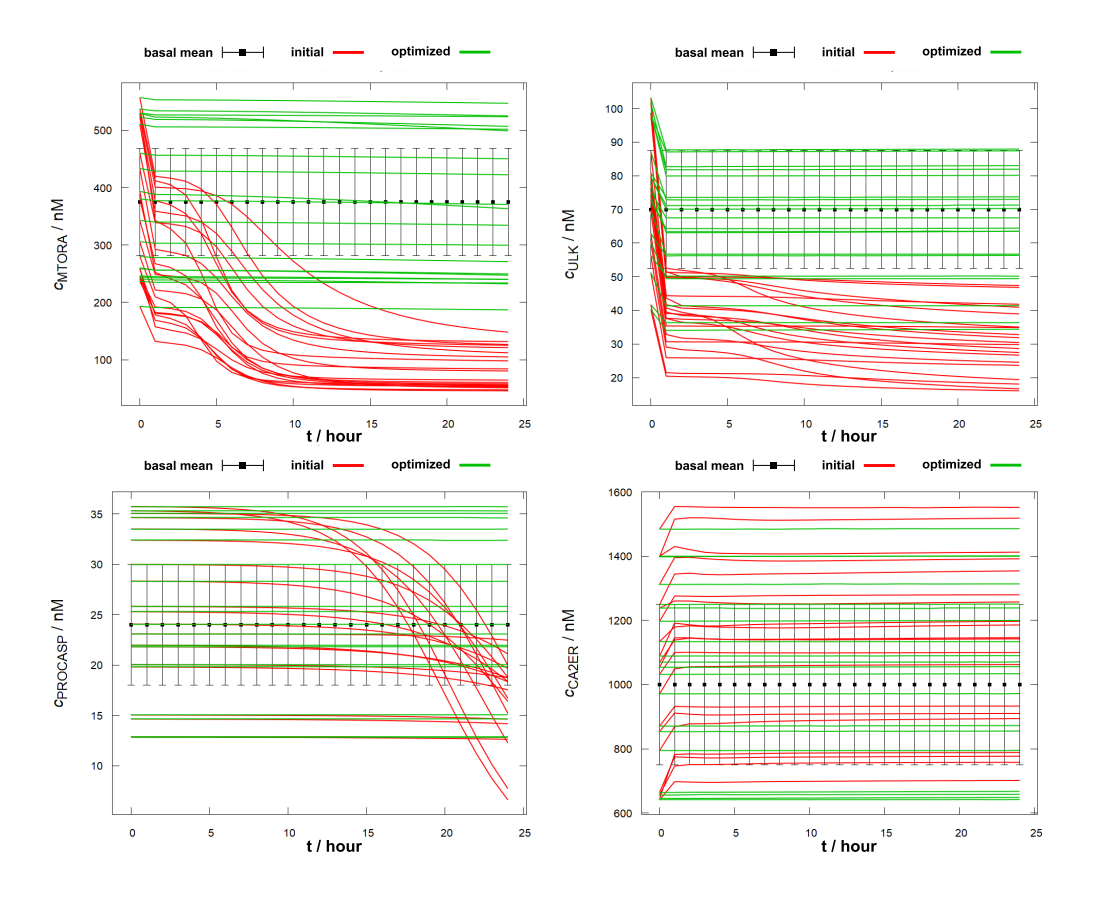


Figure 4.9: Temporal concentration profiles of key regulatory species from 20 random initial conditions within the basal range $[c_s^{\text{mean}} \pm 4\sigma_s]$ for the initial (red) and optimized (green) models over 24 h. Shaded areas represent $c_s^{\text{mean}} \pm 2\sigma_s$. MTORA (active mTOR, upper left) maintains elevated levels in the optimized model, indicating nutrient-rich conditions. ULK (inactive ULK1, upper right) remains high, confirming autophagy suppression. PROCASP (procaspase, lower left) stays constant, demonstrating absent apoptotic signaling. CA2ER (ER calcium, lower right) shows proper calcium homeostasis with characteristically high ER concentrations. The optimized model (green) successfully maintains physiological homeostasis, while the initial model (red) fails to sustain basal conditions. Adapted from [142].

5 Discussion

Autophagy is an essential cellular survival mechanism activated in response to various intracellular or extracellular stressors. Dysregulation of autophagy has been implicated in numerous diseases, including cancer, where it exhibits a dual role, and neurodegenerative disorders [27, 28, 29, 134, 135]. This makes autophagy a compelling target for precision medicine [152, 153]. While high-throughput multi-omics methods generate substantial data and have enabled significant advancements, models derived from these approaches often struggle to accurately predict responses in small groups of individuals. This difficulty primarily stems from the "high-dimension, low-sample-size" (HDLSS) dilemma, where the vast number of measured variables contrasts sharply with limited data availability a situation particularly prevalent in studies involving rare diseases [154, 155, 156]. The challenge of high-dimension, low-sample-size (HDLSS) data underscores the limitations of purely data-driven predictive models. In contrast, quantitative mechanistic models leverage established biological principles and interaction networks to elucidate the underlying dynamics of cellular systems [157]. This focus on dynamical insight offers a significant advantage: the mechanistic framework can reduce the extensive data requirements typically needed for model calibration and prediction, a benefit particularly relevant in data-scarce scenarios [158, 159].

We have built upon a mechanistic modeling approach, advancing on prior autophagy models to further investigate the detailed dynamics of ULK1-mediated autophagy induction. Initial qualitative dynamical analyses (including bifurcation and phase plane analysis) of the base model indicated a need for expansion to accurately capture a broader range of molecular biological behaviors.

Consequently, this work transitioned from our group's established reductionist strategy, which typically examines individual molecular interactions in isolation, towards a more integrative, top-down methodology. This involved embedding our validated small-scale model within a more comprehensive, existing autophagy-apoptosis network. This approach posed considerable challenges, as the target extensive model lacked readily usable parameterization and initial conditions, necessitating its effective reconstruction from the ground up. To address the complexities of parameter estimation and uncertainty quantification

for this expanded system, we leveraged the Optima++ framework. This marked a novel application of Optima++, a framework primarily designed for combustion kinetics, to the domain of biochemical reaction systems. The adoption of Optima++ provided significant methodological advantages, notably its standardized XML data format (RKD) that facilitates systematic data handling, alongside access to a range of advanced numerical tools for optimization and analysis. As a result of this approach, the newly developed and integrated model is now capable of simulating a homeostatic cellular state while retaining the core mechanisms of our previous small-scale model, thus offering a more powerful and comprehensive platform for future investigations into autophagy.

5.1 Integration of Experimental Design and Computational Modeling

A significant methodological contribution of this research is the development of a pipeline connecting wet-lab experimental design with dry-lab computational modeling. The PP2A study exemplifies this integrated approach, where we demonstrated that a well designed in-vitro experiment generated time-series data can be suited for model parameterization despite the challenges of sparse, highly noisy biological measurements. The experimental design focused on time-course measurements capturing the phosphorylation dynamics of key network components (p70S6K for mTORC1 activity, ULK1-Ser757, and PP2A-Tyr307) following targeted perturbations with rapamycin or okadaic acid. With this relatively simple approach we were able to generate Quantitative readouts. This relatively simple approach was able to follow network state changes over time, providing essential constraints for parameter estimation.

As part of our data processing strategy, we fitted polynomial functions to the experimental time-series data, an approach known as data smoothing [160]. These continuous polynomial functions effectively captured underlying temporal trends while mitigating the inherent noise characteristic of western blot measurements. We then sampled from these functions at a higher frequency than the original experimental measurements. This step generated densely sampled pseudo-data points that not only preserved the essential underlying dynamics but also further reduced the impact of experimental variability. This overall approach significantly improved the robustness of parameter estimation by providing more consistent and refined constraints for the optimization algorithms, while ensuring fidelity to the initial experimental observations. The statistical analysis methodology, incorporating multiple normalization steps and replicate experiments, further helped mitigate the inherent variability in western blot quantification, a common challenge in systems biology modeling. By implementing independent validation experiments distinct from those used for fitting

(combined treatments with siRNA knockdowns), the model predictive capacity was tested. This validation strategy represents an important advance in model development practice, as it confirms the model's ability to predict system behaviors under conditions not used for its parameterization.

5.2 Oscillatory Dynamics Require Time-Delayed Negative Feedback

Dynamical analysis of the optimized model revealed that the system exhibits bistability due to the interplay of positive (ULK1 \rightarrow PP2A \rightarrow ULK1) and double-negative (mTORC1 \dashv ULK1 \dashv mTORC1, mTORC1 \dashv PP2A \dashv mTORC1) feedback loops. This bistable characteristic enables robust decision-making, where rapamycin treatment forces a transition from "Non-autophagy state" to "Autophagy state" by removing the physiological stable steady state, while OA treatment preserves bistability while preventing autophagy activation under normal conditions.

On the contrary, we observed similar oscillatory behavior under specific concentrations of okadaic acid (OA) treatment (e.g., 100 nM for 180 minutes), indicating a temporal control mechanism that has not been extensively characterized. This discovery aligned with our group's previous experiments with rapamycin treatment [50, 140]. These findings prompted me to conduct an extensive dynamical systems analysis on our group's base ULK1-mTORC1-AMPK model, which has essentially the same structure as the PP2A model introduced here. These findings prompted an extensive dynamical systems analysis on our group's base ULK1-mTORC1-AMPK model, which has essentially the same structure as the PP2A model introduced here. The dynamical system analysis showed that the core AMPK-mTORC1-ULK1 network, despite its multiple feedback loops, cannot sustain these oscillations without a critical additional component: a significant time delay within a negative feedback loop.

To test our hypothesis, we introduced an intermediary regulatory protein (REG) that mediates certain effects of AMPK on ULK1 and mTORC1. This modified model successfully reproduced the sustained oscillations observed experimentally under various conditions, including starvation and rapamycin treatments, thereby aligning with a broader range of our experimental observations. This introduced delay, in the REG-mediated pathway, is crucial, as the periodic inactivation in the system makes it possible to switch off autophagy when it's no longer necessary. Global sensitivity analysis further confirmed the importance of this delay pathway; parameters governing the AMPK-REG interaction ranked as the fourth most significant in impacting system dynamics, surpassed in importance only by the overall stress level and the maximum activity and concentration of AMPK.

The biological significance of these oscillations likely relates to cellular resource allocation. Periodic autophagy activation allows cells to alternate between degradation phases (when autophagy is active) and utilization phases (when mTORC1 reactivates), enabling efficient recycling of cellular components without overwhelming the cell's metabolic capacity.

5.3 From Minimal Models to Comprehensive Networks

To extend our investigations into a broader cellular context, we developed a more comprehensive autophagy-apoptosis model. This work was initially based on the model proposed by Liu et al. [120]; however, significant modifications and an entirely new parameter estimation were necessitated due to the unavailability of their source code and protein concentrations used, which prevented reproduction of their published results. A primary objective for our revised baseline model was to achieve stable homeostatic behavior under unperturbed conditions, as the model with the published parameter values converged rapidly towards apoptotic states irrespective of initial conditions. This extensive recalibration and development process aimed to establish a foundational resource for studying broader cellular decision-making. The resulting model, containing parameters derived from its 113 reactions, presented a significant optimization challenge due to its high dimensionality. To address this, we first established a plausible initial concentration range and sampling strategy for each species by integrating methods and simplifications from published models of similar biological processes. Following this, and prior to full optimization, local sensitivity analysis was employed to pragmatically reduce dimensionality. This analysis identified 101 influential parameters using the SUE impact measure, which effectively ranked parameter influence by considering sensitivity, initial uncertainty, and experimental error factors. For the subsequent high-dimensional parameter optimization, we adopted an innovative approach by transferring methodologies from combustion kinetics. Specifically, we utilized the Optima++ FOCTOPUS (FOCusing robusT Optimization with Uncertainty-based Sampling) algorithm, employing the Cantera solver. This cross-disciplinary application of the Optima++ framework, originally designed for combustion kinetics, proved effective for this biological system, successfully managing the complex parameter space and dramatically reducing the overall Root Mean Square Deviation (RMSD) error from approximately 1.3×10^9 to 2.22.

Particularly noteworthy in our calibration pipeline was the rigorous posterior uncertainty analysis performed on the optimized parameters. This quantified the reduction in parameter uncertainty achieved through calibration, thereby providing a more robust foundation for future model iterations by explicitly characterizing the confidence associated

with each parameter. For instance, this analysis revealed that parameters related to 19 reactions could be constrained to within one order of magnitude ($f_{posterior} < 1$), while others remained less certain. Such findings offer invaluable guidance for designing targeted experimental studies aimed at further model refinement. These thorough posterior investigations were especially crucial given the sheer volume of initially unknown parameters and the inherent uncertainties regarding exact cellular protein concentrations.

This work provides comprehensive documentation of the model development process, including detailed specifications of initial concentration ranges, reaction modifications, and optimization procedures. The complete computational implementation is made available through GitHub repositories:

- https://github.com/mcsksgyrk/basal_state_calibi
- https://github.com/eraut/pp2aMtorUlk
- https://github.com/eraut/Autophagy_oscillation

to ensure reproducibility and enable extension by other researchers. This open access approach facilitates model reuse and validation within the systems biology community.

5.3.1 Future Directions

While the current model accurately simulates basal autophagy behavior, realizing its full predictive capabilities for autophagy regulation across diverse cellular stress conditions necessitates further development. A primary challenge in this endeavor is achieving high certainty in parameter estimation, a task which requires extensive quantitative data and rigorous calibration procedures [137]. Ongoing refinement efforts are therefore focused on expanding the model's predictive scope beyond these initial homeostatic scenarios. A cornerstone of this advancement is the systematic compilation of experimental data from numerous literature sources into the standardized "ReSpecTh Kinetic Data" (RKD) XML format. This structured data curation represents a significant methodological improvement, essential for facilitating more robust parameter optimization and rigorous validation of complex biological models, particularly when employing advanced computational frameworks for systems biology.

Using this structured database, we plan to optimize the model to reproduce multiple experimental conditions, particularly focusing on rapamycin treatment and various starvation protocols. The approach presented in this thesis offers unique advantages for this ongoing work, as the Optima++ framework can simultaneously utilize multiple XML data sources for simulations and parameter fitting. This capability provides a robust platform for model

evolution, where reactions can be added or removed while maintaining the model's ability to reproduce previously validated behaviors.

A particularly valuable aspect of this methodology is that after modification of the reaction network, the model can be re-optimized using the exact same initial concentration ranges and measurement data. This ensures that features and behaviors validated in earlier iterations are preserved in subsequent model versions. Such continuity in model development is essential for gradually building more comprehensive representations of complex biological systems without sacrificing previously achieved accuracies.

The extension of the model to simulate stress responses will provide deeper insights into autophagy regulation under pathological conditions. By incorporating data from diverse experimental paradigms into a unified modeling framework, we aim to develop a more integrative understanding of how the autophagy-apoptosis decision network functions across different cellular contexts and stress conditions. This work will further strengthen the model's utility for predicting therapeutic interventions in autophagy-related diseases and provide a more comprehensive platform for investigating the complex dynamics of cellular stress responses.

6 Conclusions

This thesis has investigated ULK1-mediated autophagy regulatory mechanisms using systems biology approaches, effectively addressing the objectives outlined for this research.

- A small-scale chemical reaction network model was developed incorporating PP2A
 and its connections to ULK1 and mTORC1, capturing essential regulatory interactions within this network. The approach integrated classical molecular biology
 methods with computational modeling in a complementary manner. Structural identifiability analysis guided experimental design, ensuring model identifiability, and
 these targeted experiments enabled determination of previously unknown reaction
 rates.
- This work established that highly variable western blot data can provide sufficient constraints for parameter estimation when combined with appropriate experimental design and data processing strategies. Experimental time-series tracking phosphory-lation states of key network components (p70S6K, ULK1-Ser757, PP2A-Tyr307) following rapamycin or okadaic acid treatments provided essential constraints for parameter optimization. The model's predictive capability was validated using independent experiments not included in the parameter fitting process, following rigorous model development protocols.
- Model analysis revealed the necessity of an intermediary regulatory component (REG) for oscillatory autophagy dynamics. Systematic disruption of REG's dual functions abolished both oscillations and proper autophagy induction, with the system settling into inappropriate steady states. Global sensitivity analysis using the Sobol method confirmed the structural importance of this delay mechanism, identifying AMPK-REG interactions among the most influential parameters for system dynamics. These findings suggests that biologically realistic autophagy models require additional state variables beyond the core AMPK-mTORC1-ULK1 network to capture the temporal complexity observed experimentally.
- An open-source, comprehensive autophagy-apoptosis model was developed through extensive modification of Liu et al.'s framework [120], necessitated by the original

model's lack of reproducibility due to missing source code and initial concentrations. The reconstructed model achieves stable homeostatic behavior under basal conditions.

- To address the complexity of this 113-reaction network, physiologically plausible concentration ranges were established by integrating data from multiple published models. This work pioneered the application of Optima++ to biochemical reaction networks, transferring advanced computational methods from combustion kinetics to systems biology. Local sensitivity analysis using the *SUE* impact measure identified 101 influential parameters from the full parameter space. Subsequent optimization with the FOCTOPUS algorithm achieved a dramatic reduction in RMSD error from 1.3×10^9 to 2.22.
- This systematic calibration approach constrained 19 key reaction parameters to
 within one order of magnitude without requiring direct experimental measurements
 for this foundational phase. These parameter bounds provide essential guidance for
 future experimental design and targeted model refinement toward clinically relevant
 applications.

The comprehensive documentation of all model implementations, including detailed specifications of concentration ranges, reaction modifications, and analysis procedures, follows the new standards for reproducibility in computational science. The methodological framework developed here creates a foundation for future translational applications. However, achieving clinical relevance will require systematic integration of quantitative experimental data and validation across diverse physiological and pathological conditions. All models and analysis tools are publicly available in GitHub repositories, ensuring accessibility and enabling the broader scientific community to build upon this work.

7 Summary

In this PhD thesis, we contributed significant insights into the dynamical regulation of ULK1-mediated autophagy induction through innovative systems biology approaches.

We developed an experimental-computational pipeline that utilizes noisy western blot time-series data for parameter estimation in dynamic models. This methodology enabled us to construct a chemical reaction network model incorporating PP2A, ULK1, and mTORC1 interactions that successfully predicted cellular responses to treatments not used in our parameterization.

We made important discoveries about autophagy oscillations, observing periodic activation at specific concentrations of rapamycin and okadaic acid. Through phase plane analysis, we demonstrated that models without time delay could not reproduce these dynamics. We proved this by incorporating an intermediary regulatory component mediating some of AMPK's effects on both ULK1 and mTORC1, establishing that AMPK had to exert part of its regulatory influence through this intermediary protein for the system to exhibit oscillations.

To extend our computational domain, we developed a comprehensive autophagy-apoptosis model by extensively modifying an existing framework from Liu et al. We applied state-of-the-art computational methods and tools to address the complex challenges of biological systems modeling. We repurposed the Optima++ computational framework for biochemical reaction networks, using Optima++ for the first time outside of combustion kinetics. Our approach combined local sensitivity analysis using the SUE impact measure to identify influential parameters, which we then optimized using the advanced FOCTOPUS algorithm. We established a new standard for utilizing multiple data sources in biochemical reaction network parameter optimization through the standardized ReSpecTh XML format, enabling systematic compilation and integration of experimental data from diverse literature sources.

These mechanistic insights provide a foundation for understanding autophagy dysregulation in diseases such as cancer, neurodegeneration, and metabolic disorders, potentially informing future therapeutic interventions targeting this crucial cellular process.

8 References

- [1] Levine B, Kroemer G. Autophagy in the pathogenesis of disease. Cell. 2008;132(1):27-42.
- [2] Jin S. Autophagy, mitochondrial quality control, and oncogenesis. Autophagy. 2006;2(2):80-4.
- [3] Cao W, Li J, Yang K, Cao D. An overview of autophagy: Mechanism, regulation and research progress. Bulletin du cancer. 2021;108(3):304-22.
- [4] Zoncu R, Efeyan A, Sabatini DM. mTOR: from growth signal integration to cancer, diabetes and ageing. Nature reviews Molecular cell biology. 2011;12(1):21-35.
- [5] Kitada M, Koya D. Autophagy in metabolic disease and ageing. Nature Reviews Endocrinology. 2021;17(11):647-61.
- [6] Yin Z, Pascual C, Klionsky DJ. Autophagy: machinery and regulation. Microbial cell. 2016;3(12):588.
- [7] Wirawan E, Berghe TV, Lippens S, Agostinis P, Vandenabeele P. Autophagy: for better or for worse. Cell research. 2012;22(1):43-61.
- [8] Garcia D, Shaw RJ. AMPK: mechanisms of cellular energy sensing and restoration of metabolic balance. Molecular cell. 2017;66(6):789-800.
- [9] Hardie DG, Ross FA, Hawley SA. AMPK: a nutrient and energy sensor that maintains energy homeostasis. Nature reviews Molecular cell biology. 2012;13(4):251-62.
- [10] Mihaylova MM, Shaw RJ. The AMPK signalling pathway coordinates cell growth, autophagy and metabolism. Nature cell biology. 2011;13(9):1016-23.
- [11] Eskelinen EL. Autophagy: supporting cellular and organismal homeostasis by self-eating. The international journal of biochemistry & cell biology. 2019;111:1-10.

- [12] Yuan J, Ofengeim D. A guide to cell death pathways. Nature Reviews Molecular Cell Biology. 2024;25(5):379-95.
- [13] Gómez-Virgilio L, Silva-Lucero MdC, Flores-Morelos DS, Gallardo-Nieto J, Lopez-Toledo G, Abarca-Fernandez AM, et al. Autophagy: a key regulator of homeostasis and disease: an overview of molecular mechanisms and modulators. Cells. 2022;11(15):2262.
- [14] Menzies FM, Fleming A, Rubinsztein DC. Compromised autophagy and neurodegenerative diseases. Nature Reviews Neuroscience. 2015;16(6):345-57.
- [15] Wu J, Xu W, Su Y, Wang Gh, Ma Jj. Targeting chaperone-mediated autophagy in neurodegenerative diseases: mechanisms and therapeutic potential. Acta pharmacologica Sinica. 2025;46(4):816-28.
- [16] Natale G, Lenzi P, Lazzeri G, Falleni A, Biagioni F, Ryskalin L, et al. Compartment-dependent mitochondrial alterations in experimental ALS, the effects of mitophagy and mitochondriogenesis. Frontiers in Cellular Neuroscience. 2015;9:434.
- [17] Ueno T, Komatsu M. Autophagy in the liver: functions in health and disease. Nature reviews Gastroenterology & hepatology. 2017;14(3):170-84.
- [18] Gukovskaya AS, Gukovsky I, Algül H, Habtezion A. Autophagy, inflammation, and immune dysfunction in the pathogenesis of pancreatitis. Gastroenterology. 2017;153(5):1212-26.
- [19] Biczo G, Vegh ET, Shalbueva N, Mareninova OA, Elperin J, Lotshaw E, et al. Mitochondrial dysfunction, through impaired autophagy, leads to endoplasmic reticulum stress, deregulated lipid metabolism, and pancreatitis in animal models. Gastroenterology. 2018;154(3):689-703.
- [20] Li H, Li D, Ma Z, Qian Z, Kang X, Jin X, et al. Defective autophagy in osteoblasts induces endoplasmic reticulum stress and causes remarkable bone loss. Autophagy. 2018;14(10):1726-41.
- [21] Lassen KG, Xavier RJ. Mechanisms and function of autophagy in intestinal disease. Autophagy. 2018;14(2):216-20.
- [22] Alula KM, Theiss AL. Autophagy in crohn's disease: converging on dysfunctional innate immunity. Cells. 2023;12(13):1779.
- [23] Shao BZ, Yao Y, Zhai JS, Zhu JH, Li JP, Wu K. The role of autophagy in inflammatory bowel disease. Frontiers in Physiology. 2021;12:621132.

- [24] Bonaldo P, Sandri M. Cellular and molecular mechanisms of muscle atrophy. Disease models & mechanisms. 2013;6(1):25-39.
- [25] Du J, Li Y, Zhao W. Autophagy and myocardial ischemia. Autophagy: Biology and Diseases: Clinical Science. 2020:217-22.
- [26] Yamaguchi O. Autophagy in the heart. Circulation Journal. 2019;83(4):697-704.
- [27] Verma AK, Bharti PS, Rafat S, Bhatt D, Goyal Y, Pandey KK, et al. Autophagy paradox of cancer: Role, regulation, and duality. Oxidative Medicine and Cellular Longevity. 2021;2021(1):8832541.
- [28] Mohammed WH, Sulaiman GM, Abomughaid MM, Klionsky DJ, Abu-Alghayth MH. The dual role of autophagy in suppressing and promoting hepatocellular carcinoma. Frontiers in Cell and Developmental Biology. 2024;12:1472574.
- [29] Singh SS, Vats S, Chia AYQ, Tan TZ, Deng S, Ong MS, et al. Dual role of autophagy in hallmarks of cancer. Oncogene. 2018;37(9):1142-58.
- [30] Rao S, Tortola L, Perlot T, Wirnsberger G, Novatchkova M, Nitsch R, et al. A dual role for autophagy in a murine model of lung cancer. Nature communications. 2014;5(1):3056.
- [31] Galluzzi L, Bravo-San Pedro JM, Levine B, Green DR, Kroemer G. Pharmacological modulation of autophagy: therapeutic potential and persisting obstacles. Nature reviews Drug discovery. 2017;16(7):487-511.
- [32] Luo M, Ye L, Chang R, Ye Y, Zhang Z, Liu C, et al. Multi-omics characterization of autophagy-related molecular features for therapeutic targeting of autophagy. Nature Communications. 2022;13(1):6345.
- [33] Jacomin AC, Gul L, Sudhakar P, Korcsmaros T, Nezis IP. What we learned from big data for autophagy research. Frontiers in cell and developmental biology. 2018;6:92.
- [34] Sarmah DT, Bairagi N, Chatterjee S. Tracing the footsteps of autophagy in computational biology. Briefings in Bioinformatics. 2021;22(4):bbaa286.
- [35] Tavassoly I, Parmar J, Shajahan-Haq A, Clarke R, Baumann WT, Tyson JJ. Dynamic modeling of the interaction between autophagy and apoptosis in mammalian cells. CPT: pharmacometrics & systems pharmacology. 2015;4(4):263-72.
- [36] Dalchau N, Szép G, Hernansaiz-Ballesteros R, Barnes CP, Cardelli L, Phillips A, et al. Computing with biological switches and clocks. Natural computing. 2018;17(4):761-79.

- [37] Tyson JJ, Chen KC, Novak B. Sniffers, buzzers, toggles and blinkers: dynamics of regulatory and signaling pathways in the cell. Current opinion in cell biology. 2003;15(2):221-31.
- [38] Shirin A, Klickstein IS, Feng S, Lin YT, Hlavacek WS, Sorrentino F. Prediction of optimal drug schedules for controlling autophagy. Scientific reports. 2019;9(1):1428.
- [39] Shi Q, Pei F, Silverman GA, Pak SC, Perlmutter DH, Liu B, et al. Mechanisms of action of autophagy modulators dissected by quantitative systems pharmacology analysis. International journal of molecular sciences. 2020;21(8):2855.
- [40] Alers S, Löffler AS, Wesselborg S, Stork B. Role of AMPK-mTOR-Ulk1/2 in the regulation of autophagy: cross talk, shortcuts, and feedbacks. Molecular and cellular biology. 2012;32(1):2-11.
- [41] Hosokawa N, Sasaki T, Iemura Si, Natsume T, Hara T, Mizushima N. Atg101, a novel mammalian autophagy protein interacting with Atg13. Autophagy. 2009;5(7):973-9.
- [42] Wong PM, Puente C, Ganley IG, Jiang X. The ULK1 complex: sensing nutrient signals for autophagy activation. Autophagy. 2013;9(2):124-37.
- [43] Gong Q, Wang H, Yu P, Qian T, Xu X. Protective or harmful: the dual roles of autophagy in diabetic retinopathy. Frontiers in Medicine. 2021;8:644121.
- [44] Jewell JL, Russell RC, Guan KL. Amino acid signalling upstream of mTOR. Nature reviews Molecular cell biology. 2013;14(3):133-9.
- [45] Inoki K, Li Y, Zhu T, Wu J, Guan KL. TSC2 is phosphorylated and inhibited by Akt and suppresses mTOR signalling. Nature cell biology. 2002;4(9):648-57.
- [46] Manning BD, Tee AR, Logsdon MN, Blenis J, Cantley LC. Identification of the tuberous sclerosis complex-2 tumor suppressor gene product tuberin as a target of the phosphoinositide 3-kinase/akt pathway. Molecular cell. 2002;10(1):151-62.
- [47] Sengupta S, Peterson TR, Sabatini DM. Regulation of the mTOR complex 1 pathway by nutrients, growth factors, and stress. Molecular cell. 2010;40(2):310-22.
- [48] Bai X, Jiang Y. Key factors in mTOR regulation. Cellular and molecular life sciences. 2010;67:239-53.
- [49] Laplante M, Sabatini DM. mTOR signaling in growth control and disease. cell. 2012;149(2):274-93.

- [50] Holczer M, Hajdú B, Lőrincz T, Szarka A, Bánhegyi G, Kapuy O. A Double Negative Feedback Loop between mTORC1 and AMPK Kinases Guarantees Precise Autophagy Induction upon Cellular Stress. International Journal of Molecular Sciences. 2019 Nov;20(22):5543.
- [51] Holczer M, Hajdú B, Lőrincz T, Szarka A, Bánhegyi G, Kapuy O. A double negative feedback loop between mTORC1 and AMPK kinases guarantees precise autophagy induction upon cellular stress. International journal of molecular sciences. 2019;20(22):5543.
- [52] Høyer-Hansen M, Bastholm L, Szyniarowski P, Campanella M, Szabadkai G, Farkas T, et al. Control of macroautophagy by calcium, calmodulin-dependent kinase kinase-β, and Bcl-2. Molecular cell. 2007;25(2):193-205.
- [53] Gwinn DM, Shackelford DB, Egan DF, Mihaylova MM, Mery A, Vasquez DS, et al. AMPK phosphorylation of raptor mediates a metabolic checkpoint. Molecular cell. 2008;30(2):214-26.
- [54] Hajdú B, Holczer M, Horváth G, Szederkényi G, Kapuy O. Fine-Tuning of mTORC1-ULK1-PP2A Regulatory Triangle Is Crucial for Robust Autophagic Response upon Cellular Stress. Biomolecules. 2022;12(11):1587.
- [55] Kim J, Kundu M, Viollet B, Guan KL. AMPK and mTOR regulate autophagy through direct phosphorylation of Ulk1. Nature cell biology. 2011;13(2):132-41.
- [56] Ling NX, Kaczmarek A, Hoque A, Davie E, Ngoei KR, Morrison KR, et al. mTORC1 directly inhibits AMPK to promote cell proliferation under nutrient stress. Nature metabolism. 2020;2(1):41-9.
- [57] Löffler AS, Alers S, Dieterle AM, Keppeler H, Franz-Wachtel M, Kundu M, et al. Ulk1-mediated phosphorylation of AMPK constitutes a negative regulatory feedback loop. Autophagy. 2011;7(7):696-706.
- [58] Dunlop EA, Hunt DK, Acosta-Jaquez HA, Fingar DC, Tee AR. ULK1 inhibits mTORC1 signaling, promotes multisite Raptor phosphorylation and hinders substrate binding. Autophagy. 2011;7(7):737-47.
- [59] Jung CH, Seo M, Otto NM, Kim DH. ULK1 inhibits the kinase activity of mTORC1 and cell proliferation. Autophagy. 2011;7(10):1212-21.
- [60] Novak B, Kapuy O, Domingo-Sananes MR, Tyson JJ. Regulated protein kinases and phosphatases in cell cycle decisions. Current opinion in cell biology. 2010;22(6):801-8.

- [61] Shi Y. Serine/threonine phosphatases: mechanism through structure. Cell. 2009;139(3):468-84.
- [62] Amin P, Awal S, Vigneron S, Roque S, Mechali F, Labbé JC, et al. PP2A-B55: substrates and regulators in the control of cellular functions. Oncogene. 2022;41(1):1-14.
- [63] Di Conza G, Cafarello ST, Loroch S, Mennerich D, Deschoemaeker S, Di Matteo M, et al. The mTOR and PP2A pathways regulate PHD2 phosphorylation to fine-tune HIF1α levels and colorectal cancer cell survival under hypoxia. Cell reports. 2017;18(7):1699-712.
- [64] Kuo YC, Huang KY, Yang CH, Yang YS, Lee WY, Chiang CW. Regulation of phosphorylation of Thr-308 of Akt, cell proliferation, and survival by the B55 α regulatory subunit targeting of the protein phosphatase 2A holoenzyme to Akt. Journal of Biological Chemistry. 2008;283(4):1882-92.
- [65] Shang L, Chen S, Du F, Li S, Zhao L, Wang X. Nutrient starvation elicits an acute autophagic response mediated by Ulk1 dephosphorylation and its subsequent dissociation from AMPK. Proceedings of the National Academy of Sciences. 2011;108(12):4788-93.
- [66] Wong PM, Feng Y, Wang J, Shi R, Jiang X. Regulation of autophagy by coordinated action of mTORC1 and protein phosphatase 2A. Nature communications. 2015;6(1):1-11.
- [67] Hartley D, Cooper GM. Role of mTOR in the degradation of IRS-1: regulation of PP2A activity. Journal of cellular biochemistry. 2002;85(2):304-14.
- [68] Peterson RT, Desai BN, Hardwick JS, Schreiber SL. Protein phosphatase 2A interacts with the 70-kDa S6 kinase and is activated by inhibition of FKBP12–rapamycinassociated protein. Proceedings of the National Academy of Sciences. 1999;96(8):4438-42.
- [69] Asnaghi L, Bruno P, Priulla M, Nicolin A. mTOR: a protein kinase switching between life and death. Pharmacological research. 2004;50(6):545-9.
- [70] Hu Z, Sankar DS, Vu B, Leytens A, Vionnet C, Wu W, et al. ULK1 phosphory-lation of striatin activates protein phosphatase 2A and autophagy. Cell Reports. 2021;36(13):109762.

- [71] Sun Q, Wei LL, Zhang M, Li TX, Yang C, Deng SP, et al. Rapamycin inhibits activation of AMPK-mTOR signaling pathway-induced Alzheimer's disease lesion in hippocampus of rats with type 2 diabetes mellitus. International Journal of Neuroscience. 2019;129(2):179-88.
- [72] Whang YM, Kim MJ, Cho MJ, Yoon H, Choi YW, Kim TH, et al. Rapamycin enhances growth inhibition on urothelial carcinoma cells through LKB1 deficiency-mediated mitochondrial dysregulation. Journal of Cellular Physiology. 2019;234(8):13083-96.
- [73] Hawley SA, Ross FA, Gowans GJ, Tibarewal P, Leslie NR, Hardie DG. Phosphorylation by Akt within the ST loop of AMPK-α1 down-regulates its activation in tumour cells. Biochemical Journal. 2014;459(2):275-87.
- [74] Bjedov I, Toivonen JM, Kerr F, Slack C, Jacobson J, Foley A, et al. Mechanisms of life span extension by rapamycin in the fruit fly Drosophila melanogaster. Cell metabolism. 2010;11(1):35-46.
- [75] Fu Ll, Zhao Xy, Ji Ld, Xu J. Okadaic acid (OA): Toxicity, detection and detoxification. Toxicon. 2019;160:1-7.
- [76] Mizushima N, Komatsu M. Autophagy: Renovation of Cells and Tissues. Cell. 2011 Nov;147(4):728-41.
- [77] Ktistakis NT, Tooze SA. Digesting the expanding mechanisms of autophagy. Trends in cell biology. 2016;26(8):624-35.
- [78] Noda NN, Kumeta H, Nakatogawa H, Satoo K, Adachi W, Ishii J, et al. Structural basis of target recognition by Atg8/LC3 during selective autophagy. Genes to Cells. 2008;13(12):1211-8.
- [79] Abounit K, Scarabelli TM, McCauley RB. Autophagy in mammalian cells. World Journal of Biological Chemistry. 2012;3(1):1.
- [80] Glick D, Barth S, Macleod KF. Autophagy: cellular and molecular mechanisms. The Journal of Pathology. 2010 Apr;221(1):3-12.
- [81] Tanida I, Ueno T, Kominami E. LC3 and Autophagy. Autophagosome and phagosome. 2008:77-88.
- [82] Johansen T, Lamark T. Selective autophagy mediated by autophagic adapter proteins. autophagy. 2011;7(3):279-96.

- [83] Kirkin V, McEwan DG, Novak I, Dikic I. A role for ubiquitin in selective autophagy. Molecular cell. 2009;34(3):259-69.
- [84] Birgisdottir ÅB, Lamark T, Johansen T. The LIR motif—crucial for selective autophagy. Journal of cell science. 2013;126(15):3237-47.
- [85] Ichimura Y, Komatsu M. Selective degradation of p62 by autophagy. In: Seminars in immunopathology. vol. 32. Springer; 2010. p. 431-6.
- [86] Azeloglu EU, Iyengar R. Signaling networks: information flow, computation, and decision making. Cold Spring Harbor perspectives in biology. 2015;7(4):a005934.
- [87] Wen M, Spotte-Smith EWC, Blau SM, McDermott MJ, Krishnapriyan AS, Persson KA. Chemical reaction networks and opportunities for machine learning. Nature Computational Science. 2023 Jan;3(1):12-24.
- [88] Wen M, Spotte-Smith EWC, Blau SM, McDermott MJ, Krishnapriyan AS, Persson KA. Chemical reaction networks and opportunities for machine learning. Nature Computational Science. 2023;3(1):12-24.
- [89] McDermott MJ, Dwaraknath SS, Persson KA. A graph-based network for predicting chemical reaction pathways in solid-state materials synthesis. Nature communications. 2021;12(1):3097.
- [90] Aykol M, Montoya JH, Hummelshøj J. Rational solid-state synthesis routes for inorganic materials. Journal of the American Chemical Society. 2021;143(24):9244-59.
- [91] Mueller EP, Wu F, Sessions AL. Quantifying Isotopologue Reaction Networks (QIRN): a modelling tool for predicting stable isotope fractionations in complex networks. Chemical Geology. 2022;610:121098.
- [92] Blau SM, Patel HD, Spotte-Smith EWC, Xie X, Dwaraknath S, Persson KA. A chemically consistent graph architecture for massive reaction networks applied to solid-electrolyte interphase formation. Chemical science. 2021;12(13):4931-9.
- [93] Xie X, Clark Spotte-Smith EW, Wen M, Patel HD, Blau SM, Persson KA. Datadriven prediction of formation mechanisms of lithium ethylene monocarbonate with an automated reaction network. Journal of the American Chemical Society. 2021;143(33):13245-58.
- [94] Bugryniec PJ, Yeardley A, Jain A, Price N, Vernuccio S, Brown SF. Gaussian-Process based inference of electrolyte decomposition reaction networks in Li-ion

- battery failure. In: Computer Aided Chemical Engineering. vol. 51. Elsevier; 2022. p. 157-62.
- [95] Steiner M, Reiher M. Autonomous reaction network exploration in homogeneous and heterogeneous catalysis. Topics in Catalysis. 2022;65(1):6-39.
- [96] Kim Y, Kim JW, Kim Z, Kim WY. Efficient prediction of reaction paths through molecular graph and reaction network analysis. Chemical science. 2018;9(4):825-35.
- [97] Ulissi ZW, Medford AJ, Bligaard T, Nørskov JK. To address surface reaction network complexity using scaling relations machine learning and DFT calculations. Nature communications. 2017;8(1):14621.
- [98] Goitom SK, Papp M, Kovács M, Nagy T, Zsély IG, Turányi T, et al. Efficient numerical methods for the optimisation of large kinetic reaction mechanisms. Combustion Theory And Modelling. 2022;26(6):1071-97.
- [99] Müller S, Flamm C, Stadler PF. What makes a reaction network "chemical"? Journal of Cheminformatics. 2022 Sep;14(1).
- [100] Ashyraliyev M, Fomekong-Nanfack Y, Kaandorp JA, Blom JG. Systems biology: parameter estimation for biochemical models. The FEBS journal. 2009;276(4):886-902.
- [101] Almquist J, Cvijovic M, Hatzimanikatis V, Nielsen J, Jirstrand M. Kinetic models in industrial biotechnology–improving cell factory performance. Metabolic engineering. 2014;24:38-60.
- [102] Ballnus B, Schaper S, Theis FJ, Hasenauer J. Bayesian parameter estimation for biochemical reaction networks using region-based adaptive parallel tempering. Bioinformatics. 2018;34(13):i494-501.
- [103] Villaverde AF, Pathirana D, Fröhlich F, Hasenauer J, Banga JR. A protocol for dynamic model calibration. Briefings in bioinformatics. 2022;23(1):bbab387.
- [104] Whittaker DG, Clerx M, Lei CL, Christini DJ, Mirams GR. Calibration of ionic and cellular cardiac electrophysiology models. Wiley Interdisciplinary Reviews: Systems Biology and Medicine. 2020;12(4):e1482.
- [105] Tuza Z, Bandiera L, Gomez-Cabeza D, Stan G, Menolascina F. A systematic framework for biomolecular system identification. In: Proceedings of the 58th IEEE Conference on Decision and Control; 2019.

- [106] Penas DR, González P, Egea JA, Doallo R, Banga JR. Parameter estimation in large-scale systems biology models: a parallel and self-adaptive cooperative strategy. BMC bioinformatics. 2017;18:1-24.
- [107] López C. DC, Barz T, Körkel S, Wozny G. Nonlinear ill-posed problem analysis in model-based parameter estimation and experimental design. Comput Chem Eng. 2015;77:24-42.
- [108] Fröhlich F, Kaltenbacher B, Theis FJ, Hasenauer J. Scalable parameter estimation for genome-scale biochemical reaction networks. PLoS computational biology. 2017;13(1):e1005331.
- [109] Villaverde AF, Fröhlich F, Weindl D, Hasenauer J, Banga JR. Benchmarking optimization methods for parameter estimation in large kinetic models. Bioinformatics. 2019;35(5):830-8.
- [110] Balsa-Canto E, Alonso AA, Banga JR. Computational procedures for optimal experimental design in biological systems. IET systems biology. 2008;2(4):163-72.
- [111] Villaverde AF, Banga JR. Reverse engineering and identification in systems biology: strategies, perspectives and challenges. Journal of the Royal Society Interface. 2014;11(91):20130505.
- [112] Villaverde AF. Observability and structural identifiability of nonlinear biological systems. Complexity. 2019;2019(1):8497093.
- [113] Cobelli C, Distefano 3rd JJ. Parameter and structural identifiability concepts and ambiguities: a critical review and analysis. American Journal of Physiology-Regulatory, Integrative and Comparative Physiology. 1980;239(1):R7-R24.
- [114] Sher A, Niederer SA, Mirams GR, Kirpichnikova A, Allen R, Pathmanathan P, et al. A quantitative systems pharmacology perspective on the importance of parameter identifiability. Bulletin of Mathematical Biology. 2022;84(3):39.
- [115] Li J. Assessing the accuracy of predictive models for numerical data: Not r nor r2, why not? Then what? PLOS ONE. 2017 Aug;12(8):e0183250.
- [116] Tyson JJ, Novák B. Functional Motifs in Biochemical Reaction Networks. Annual Review of Physical Chemistry. 2010 Mar;61(1):219-40.
- [117] Máté Papp T, Busai Á, Zsély IG, Nagy T, Turányi T. Optima++ v2. 5: A general C++ framework for performing combustion simulations and mechanism optimization; 2024.

- [118] Zsély IG. Determination of rate parameters based on both direct and indirect measurements. International Journal of Chemical Kinetics. 2012;44(5):284-302.
- [119] Varga T, Turányi T, Czinki E, Furtenbacher T, Császár A. ReSpecTh: a joint reaction kinetics, spectroscopy, and thermochemistry information system. In: Proceedings of the 7th European Combustion Meeting. vol. 30. Citeseer; 2015. p. 1-5.
- [120] Liu B, Oltvai ZN, Bayır H, Silverman GA, Pak SC, Perlmutter DH, et al. Quantitative assessment of cell fate decision between autophagy and apoptosis. Scientific Reports. 2017 Dec;7(1).
- [121] Xu Y, Yuan J, Lipinski MM. Live imaging and single-cell analysis reveal differential dynamics of autophagy and apoptosis. Autophagy. 2013 Sep;9(9):1418-30.
- [122] Wani WY, Boyer-Guittaut M, Dodson M, Chatham J, Darley-Usmar V, Zhang J. Regulation of autophagy by protein post-translational modification. Laboratory investigation. 2015;95(1):14-25.
- [123] Racioppi L, Means AR. Calcium/calmodulin-dependent protein kinase kinase 2: roles in signaling and pathophysiology. Journal of Biological Chemistry. 2012;287(38):31658-65.
- [124] Yousefi S, Perozzo R, Schmid I, Ziemiecki A, Schaffner T, Scapozza L, et al. Calpain-mediated cleavage of Atg5 switches autophagy to apoptosis. Nature cell biology. 2006;8(10):1124-32.
- [125] Rubinsztein DC, Codogno P, Levine B. Autophagy modulation as a potential therapeutic target for diverse diseases. Nature reviews Drug discovery. 2012;11(9):709-30.
- [126] Wirawan E, Vande Walle L, Kersse K, Cornelis S, Claerhout S, Vanoverberghe I, et al. Caspase-mediated cleavage of Beclin-1 inactivates Beclin-1-induced autophagy and enhances apoptosis by promoting the release of proapoptotic factors from mitochondria. Cell death & disease. 2010;1(1):e18-8.
- [127] Pattingre S, Tassa A, Qu X, Garuti R, Liang XH, Mizushima N, et al. Bcl-2 antiapoptotic proteins inhibit Beclin 1-dependent autophagy. Cell. 2005;122(6):927-39.
- [128] Tasdemir E, Maiuri MC, Galluzzi L, Vitale I, Djavaheri-Mergny M, D'amelio M, et al. Regulation of autophagy by cytoplasmic p53. Nature cell biology. 2008;10(6):676-87.

- [129] Liu B, Bhatt D, Oltvai ZN, Greenberger JS, Bahar I. Significance of p53 dynamics in regulating apoptosis in response to ionizing radiation and polypharmacological strategies. Scientific Reports. 2014;4(1):6245.
- [130] Dalle Pezze P, Sonntag AG, Thien A, Prentzell MT, Gödel M, Fischer S, et al. A Dynamic Network Model of mTOR Signaling Reveals TSC-Independent mTORC2 Regulation. Science Signaling. 2012 Mar;5(217).
- [131] Bagci EZ, Vodovotz Y, Billiar TR, Ermentrout GB, Bahar I. Bistability in Apoptosis: Roles of Bax, Bcl-2, and Mitochondrial Permeability Transition Pores. Biophysical Journal. 2006 Mar;90(5):1546-59.
- [132] Sundaramurthy P, Gakkhar S, Sowdhamini R. Computational prediction and analysis of impact of the cross-talks between JNK and P38 kinase cascades. Bioinformation. 2009 Jan;3(6):250-4.
- [133] Tavassoly I, Parmar J, Shajahan-Haq A, Clarke R, Baumann W, Tyson J. Dynamic Modeling of the Interaction Between Autophagy and Apoptosis in Mammalian Cells. CPT: Pharmacometrics &; Systems Pharmacology. 2015 Apr;4(4):263-72.
- [134] Bloomingdale P, Karelina T, Ramakrishnan V, Bakshi S, Véronneau-Veilleux F, Moye M, et al. Hallmarks of neurodegenerative disease: A systems pharmacology perspective. CPT: Pharmacometrics & Systems Pharmacology. 2022;11(11):1399-429.
- [135] Aghamiri SS, Amin R, Helikar T. Recent applications of quantitative systems pharmacology and machine learning models across diseases. Journal of pharmacokinetics and pharmacodynamics. 2022:1-19.
- [136] Lorenzo G, Ahmed SR, Hormuth II DA, Vaughn B, Kalpathy-Cramer J, Solorio L, et al. Patient-specific, mechanistic models of tumor growth incorporating artificial intelligence and big data. Annual Review of Biomedical Engineering. 2024;26.
- [137] Qiao L, Khalilimeybodi A, Linden-Santangeli NJ, Rangamani P. The evolution of systems biology and systems medicine: From mechanistic models to uncertainty quantification. Annual Review of Biomedical Engineering. 2025;27.
- [138] Musuamba FT, Skottheim Rusten I, Lesage R, Russo G, Bursi R, Emili L, et al. Scientific and regulatory evaluation of mechanistic in silico drug and disease models in drug development: Building model credibility. CPT: Pharmacometrics & Systems Pharmacology. 2021;10(8):804-25.

- [139] An G. Specialty grand challenge: What it will take to cross the valley of death: Translational systems biology, "true" precision medicine, medical digital twins, artificial intelligence and in silico clinical trials. Frontiers Media SA; 2022.
- [140] Holczer M, Hajdú B, Lőrincz T, Szarka A, Bánhegyi G, Kapuy O. Fine-tuning of AMPK–ULK1–mTORC1 regulatory triangle is crucial for autophagy oscillation. Scientific Reports. 2020;10(1):1-12.
- [141] Hajdú B, Csabai L, Márton M, Holczer M, Korcsmáros T, Kapuy O. Oscillation of Autophagy Induction under Cellular Stress and What Lies behind It, a Systems Biology Study. International Journal of Molecular Sciences. 2023 Apr;24(8):7671.
- [142] Hajdú B, Kapuy O, Nagy T. Basal State Calibration of a Chemical Reaction Network Model for Autophagy. International Journal of Molecular Sciences. 2024;25(20):11316.
- [143] Ermentrout B, Mahajan A. Simulating, analyzing, and animating dynamical systems: a guide to XPPAUT for researchers and students. Appl Mech Rev. 2003;56(4):B53-3.
- [144] Dong R, Goodbrake C, Harrington H, G P. Differential Elimination for Dynamical Models via Projections with Applications to Structural Identifiability. SIAM Journal on Applied Algebra and Geometry. 2023;7(1):194-235. Available from: https://doi.org/10.1137/22M1469067.
- [145] Virtanen P, Gommers R, Oliphant TE, Haberland M, Reddy T, Cournapeau D, et al. SciPy 1.0: Fundamental Algorithms for Scientific Computing in Python. Nature Methods. 2020;17:261-72.
- [146] Novák B, Tyson JJ. Design principles of biochemical oscillators. Nature reviews Molecular cell biology. 2008;9(12):981-91.
- [147] Sumner T. Sensitivity analysis in systems biology modelling and its application to a multi-scale model of blood glucose homeostasis [PhD thesis]. London, UK: UCL (University College London); 2010.
- [148] Dixit VK, Rackauckas C. GlobalSensitivity. jl: Performant and Parallel Global Sensitivity Analysis with Julia. Journal of Open Source Software. 2022;7(76):4561.
- [149] Goodwin DG, Speth RL, Moffat HK, Weber BW. Cantera: An Object-oriented Software Toolkit for Chemical Kinetics, Thermodynamics, and Transport Processes; 2021. Version 2.5.1. https://www.cantera.org.

- [150] Kovács M, Papp M, Turányi T, Nagy T. A novel active parameter selection strategy for the efficient optimization of combustion mechanisms. Proceedings of the Combustion Institute. 2023;39(4):5259-67.
- [151] Pilling JT, Walker R, Warnatz J. Evaluated kinetic data for combustion modelling. J Phys Chem Ref Data. 1992;21(3).
- [152] Guhe V, Ingale P, Tambekar A, Singh S. Systems biology of autophagy in leishmanial infection and its diverse role in precision medicine. Frontiers in Molecular Biosciences. 2023;10:1113249.
- [153] Grosjean I, Roméo B, Domdom MA, Belaid A, D'Andréa G, Guillot N, et al. Autophagopathies: from autophagy gene polymorphisms to precision medicine for human diseases. Autophagy. 2022;18(11):2519-36.
- [154] Wang J, et al. Biostatistical Challenges in High-Dimensional Data Analysis: Strategies and Innovations. Computational Molecular Biology. 2024;14.
- [155] Molla G, Bitew M. Revolutionizing Personalized Medicine: Synergy with Multi-Omics Data Generation, Main Hurdles, and Future Perspectives. Biomedicines. 2024;12(12):2750.
- [156] Zhou Y, Geng P, Zhang S, Xiao F, Cai G, Chen L, et al. Multimodal functional deep learning for multiomics data. Briefings in Bioinformatics. 2024;25(5):bbae448.
- [157] Davis JD, Kumbale CM, Zhang Q, Voit EO. Dynamical systems approaches to personalized medicine. Current opinion in biotechnology. 2019;58:168-74.
- [158] Ballesta A, Gallo JM. Quantitative Systems Pharmacology: A Foundation To Establish Precision Medicine–Editorial. The Journal of Pharmacology and Experimental Therapeutics. 2023;387(1):27-30.
- [159] Pateras J, Zhang C, Majumdar S, Pal A, Ghosh P. Physics-informed machine learning for automatic model reduction in chemical reaction networks. Scientific Reports. 2025;15(1):7980.
- [160] Cleveland WS. Robust locally weighted regression and smoothing scatterplots. Journal of the American Statistical Association. 1979;74(368):829-36.
- [161] Iancu RV, Jones SW, Harvey RD. Compartmentation of cAMP Signaling in Cardiac Myocytes: A Computational Study. Biophysical Journal. 2007 May;92(9):3317-31.

- [162] Nakano T, Doi T, Yoshimoto J, Doya K. A Kinetic Model of Dopamine- and Calcium-Dependent Striatal Synaptic Plasticity. PLoS Computational Biology. 2010 Feb;6(2):e1000670.
- [163] Shin SY, Nguyen L. Unveiling Hidden Dynamics of Hippo Signalling: A Systems Analysis. Genes. 2016 Aug;7(8):44.
- [164] Hat B, Kochańczyk M, Bogdał MN, Lipniacki T. Feedbacks, Bifurcations, and Cell Fate Decision-Making in the p53 System. PLOS Computational Biology. 2016 Feb;12(2):e1004787.
- [165] Varusai TM, Nguyen LK. Dynamic modelling of the mTOR signalling network reveals complex emergent behaviours conferred by DEPTOR. Scientific Reports. 2018 Jan;8(1).
- [166] Broadbent DG, Barnaba C, Perez GI, Schmidt JC. Quantitative analysis of autophagy reveals the role of ATG9 and ATG2 in autophagosome formation. Journal of Cell Biology. 2023 Apr;222(7).
- [167] du Toit A, Hofmeyr JHS, Gniadek TJ, Loos B. Measuring autophagosome flux. Autophagy. 2018 Jul:1-12.
- [168] Bagci E, Vodovotz Y, Billiar T, Ermentrout G, Bahar I. Bistability in apoptosis: roles of bax, bcl-2, and mitochondrial permeability transition pores. Biophysical journal. 2006;90(5):1546-59.
- [169] Raychaudhuri S, Das S. Low Probability Activation of Bax/Bak Can Induce Selective Killing of Cancer Cells by Generating Heterogeneity in Apoptosis. Journal of Healthcare Engineering. 2013 Mar;4(1):47-66.
- [170] Dolan A, Diamond S. Systems Modeling of Ca2+ Homeostasis and Mobilization in Platelets Mediated by IP3 and Store-Operated Ca2+ Entry. Biophysical Journal. 2014 May;106(9):2049-60.
- [171] Lemon G, Gibson WG, Bennett MR. Metabotropic receptor activation, desensitization and sequestration—I: modelling calcium and inositol 1,4,5-trisphosphate dynamics following receptor activation. Journal of Theoretical Biology. 2003 Jul;223(1):93-111.
- [172] Wang J, Huang X, Huang W. A quantitative kinetic model for ATP-induced intracellular oscillations. Journal of Theoretical Biology. 2007 Apr;245(3):510-9.

- [173] Ashraf J, Ahmad J, Ul-Haq Z. In: Deciphering the Role of PKC in Calpain-CAST System Through Formal Modeling Approach. Springer International Publishing; 2019. p. 60-71.
- [174] Smith B, Hill C, Godfrey EL, Rand D, van den Berg H, Thornton S, et al. Dual positive and negative regulation of GPCR signaling by GTP hydrolysis. Cellular Signalling. 2009 Jul;21(7):1151-60.
- [175] Tiveci S, Akın A, Çakır T, Saybaşılı H, Ülgen K. Modelling of calcium dynamics in brain energy metabolism and Alzheimer's disease. Computational Biology and Chemistry. 2005 Apr;29(2):151-62.
- [176] Chong KH, Samarasinghe S, Kulasiri D. Mathematical modelling of p53 basal dynamics and DNA damage response. Mathematical Biosciences. 2015 Jan;259:27-42.
- [177] Geva-Zatorsky N, Rosenfeld N, Itzkovitz S, Milo R, Sigal A, Dekel E, et al. Oscillations and variability in the p53 system. Molecular Systems Biology. 2006 Jan;2(1).
- [178] Eungdamrong NJ, Iyengar R. Compartment-Specific Feedback Loop and Regulated Trafficking Can Result in Sustained Activation of Ras at the Golgi. Biophysical Journal. 2007 Feb;92(3):808-15.
- [179] Neumann L, Pforr C, Beaudouin J, Pappa A, Fricker N, Krammer PH, et al. Dynamics within the CD95 death-inducing signaling complex decide life and death of cells. Molecular Systems Biology. 2010 Jan;6(1).

9 Bibliography of the candidate's publications

Publications discussed in the dissertation:

Hajdú, Bence; Kapuy, Orsolya; Nagy, Tibor

Basal State Calibration of a Chemical Reaction Network Model for Autophagy

INTERNATIONAL JOURNAL OF MOLECULAR SCIENCES 25: 20 Paper: 11316,

18 p. (2024)

IF: 4.9

DOI: 10.3390/ijms252011316

Hajdú, Bence; Csabai, Luca*; Márton, Margita; Holczer, Marianna; Korcsmáros,

Tamás; Kapuy, Orsolya

Oscillation of Autophagy Induction under Cellular Stress and What Lies behind It, a Systems Biology Study

INTERNATIONAL JOURNAL OF MOLECULAR SCIENCES 24: 8 Paper: 7671,

16 p. (2023)

IF: 5.6

DOI: 10.3390/ijms24087671

Hajdú, Bence ; Holczer, Marianna ; Horváth, Gergely ; Szederkényi, Gábor ; Kapuy,

Orsolya

Fine-Tuning of mTORC1-ULK1-PP2A Regulatory Triangle Is Crucial for Robust

Autophagic Response upon Cellular Stress

BIOMOLECULES 12: 11 Paper: 1587, 15 p. (2022)

IF: 5.5

DOI: 10.3390/biom12111587

Publications not discussed in the dissertation:

Holczer, M.; **Hajdú, B.**; Lőrincz, T.; Szarka, A.; Bánhegyi, G.; Kapuy, O. Fine-tuning of AMPK–ULK1–mTORC1 regulatory triangle is crucial for autophagy oscillation

SCIENTIFIC REPORTS 10 : 1 Paper: 17803 , 12 p. (2020)

IF: 3.998

DOI: 10.1038/s41598-020-74825-z

Holczer, M.; **Hajdú, B.**; Lőrincz, T.; Szarka, A.; Bánhegyi, G.; Kapuy, O. A double negative feedback loop between MTORC1 and AMPK kinases guarantees precise autophagy induction upon cellular stress

INTERNATIONAL JOURNAL OF MOLECULAR SCIENCES 20 : 22 Paper: 5543, 17 p. (2019)

IF: 4.556

DOI: 10.3390/ijms20225543

10 Acknowledgments

I would like to express my sincere gratitude to my supervisor, Dr. Orsolya Kapuy, for her guidance, patience, and unwavering support throughout my doctoral journey. Her expertise and insights have been invaluable to this research.

I am grateful to the members of the Kapuy Lab for their collaboration and stimulating discussions. Special thanks to my colleagues Marianna Holczer and Margita Márton for their experimental contributions and thoughtful feedback.

I would like to express my sincere gratitude to Dr. Tibor Nagy for his exceptional guidance and expertise in computational frameworks and mathematical modeling. His insights into parameter optimization techniques and reaction kinetics were instrumental in the development of our novel methodological approaches.

I also wish to thank the Department of Molecular Medicine at Semmelweis University for providing an excellent academic environment and research facilities.

Finally, I extend my heartfelt thanks to my family and friends for their encouragement and moral support throughout my studies.

This research was supported by Richter Gedeon Talentum Fundation.

Supplementary materials

Supplementary figures

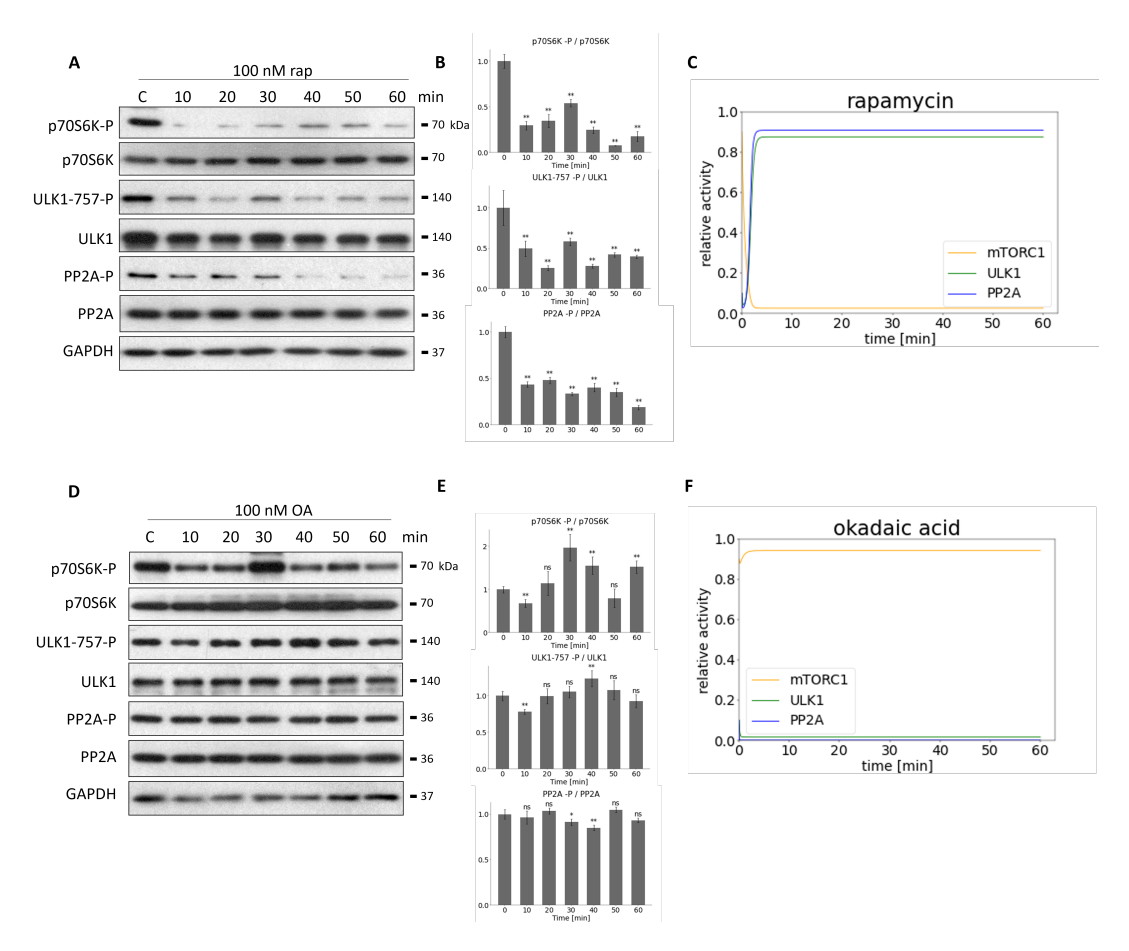


Figure S1: Experimental characterization and model simulation of mTORC1-ULK1-PP2A network response to mTORC1 and PP2A inhibition. HEK293T cells were treated over time with either 100 nM rapamycin (Rapa, top row) or 100 nM okadaic acid (OA, bottom row). (A, D) Immunoblots showing the time-dependent phosphorylation status of markers for ULK1 (ULK1-757-P), PP2A (PP2A-P), and mTORC1 (p70S6K-P), along with total protein levels. GAPDH was used as a loading control. (B, E) Densitometry data representing the relative intensity of ULK1-757-P normalized to total ULK1, PP2A-P normalized to total PP2A, and p70S6K-P normalized to total p70S6K. Data are from three independent measurements. Error bars represent standard deviation; asterisks indicate statistically significant difference from the control (time 0): ns—nonsignificant; *—p < 0.05; **—p < 0.01. In (C) and (F), the concentration changes of mTORC1, PP2A, and ULK1 over time are shown during the simulation with the optimized models[54].

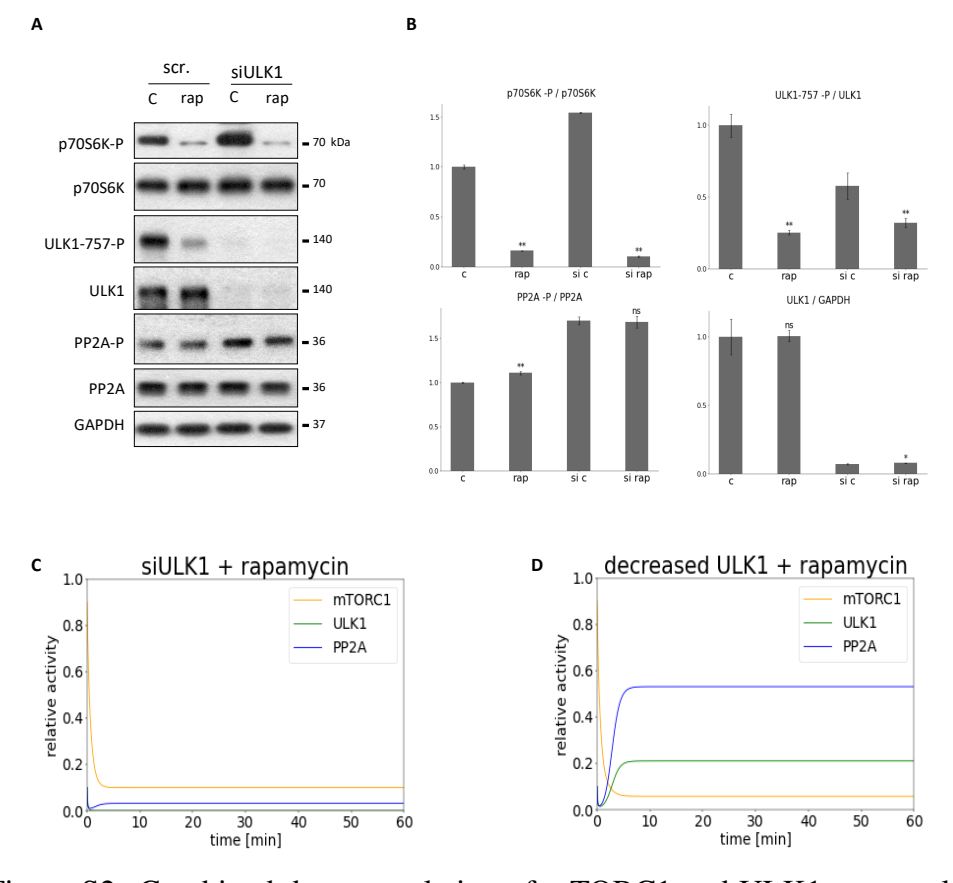


Figure S2: Combined down-regulation of mTORC1 and ULK1 can result in PP2A inhibition. ULK1 was silenced in HEK293T cells, then cells were treated with/without 100 nM rapamycin for 2 h. The silencing was checked by using a scramble siRNA. (A) The markers of ULK1 (ULK1-757-P), PP2A (PP2A-P) and mTORC1 (p70S6K-P) were followed by immunoblotting. GAPDH was used as loading control. (B) Densitometry data represent the intensity of ULK1-757-P normalized for total level of ULK1, PP2A-P normalized for total level of PP2A and p70S6K-P normalized for total level of p70S6K. For each of the experiments, three independent measurements were carried out. Error bars represent standard deviation asterisks indicate statistically significant difference from the control: ns—nonsignificant; *—p < 0.05; **—p < 0.01. The computational simulation is determined upon two different types of ULK1 silencing combined with rapamycin treatment: (C) (ULK1T = 0.01, mTORT = 0.1) and (D) (ULK1T = 0.3, mTORT = 0.1). The relative activity of mTORC1, PP2A, ULK1 is shown. Figure taken from our previous work [54].

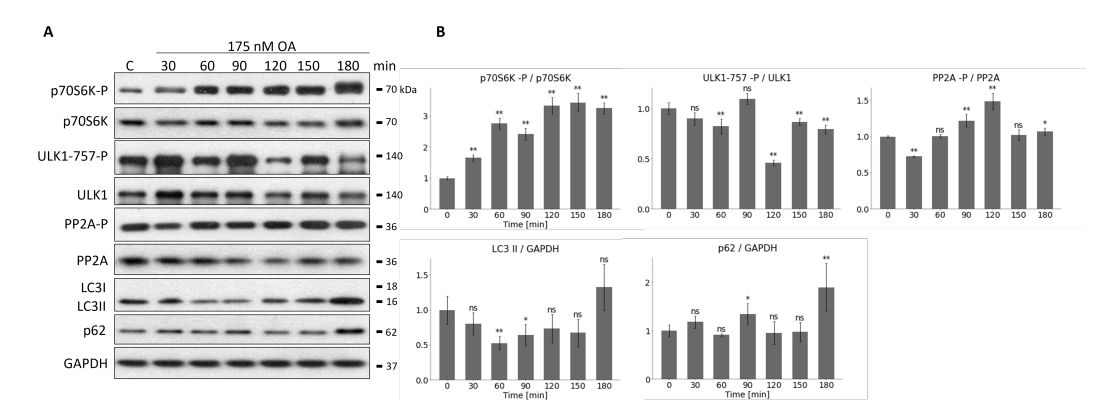


Figure S3: High concentration Okadaic Acid treatment does not induce oscillatory protein dynamics. (A) HEK293T cells were treated over time with 175 nM okadaic acid (OA) for 180 min. Markers for mTORC1 activity (p70S6K-P), ULK1 phosphorylation (ULK1-757-P), PP2A phosphorylation (PP2A-P), and autophagy (LC3I/II, p62) were assessed by immunoblotting. Total protein levels and GAPDH were used as loading controls. (B) Densitometry data corresponding to panel A. Intensities of phosphorylated proteins (p70S6K-P, ULK1-757-P, PP2A-P) were normalized to their respective total protein levels. LC3II and p62 intensities were normalized to GAPDH. Data represent mean \pm SD (n=3). Asterisks indicate statistically significant difference from the control (time 0): ** p < 0.01, * p < 0.05; ns: non-significant. Figure taken from our previous work [54].

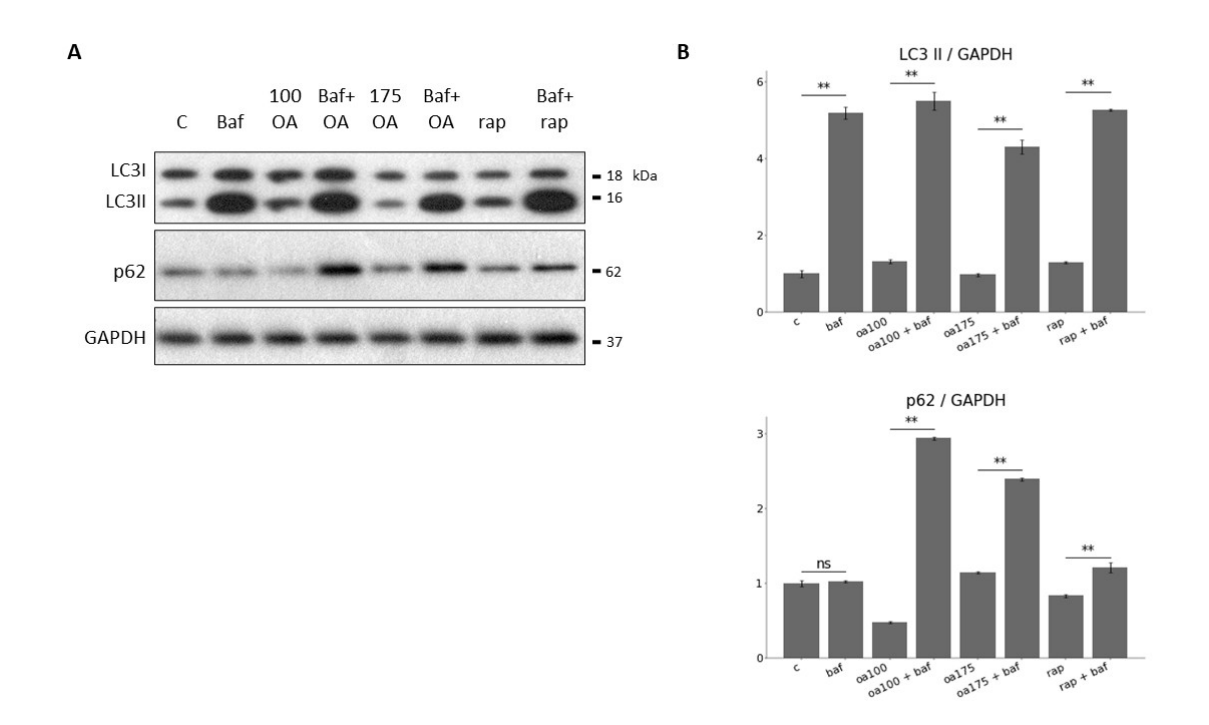


Figure S4: Analysing OA induced autophagy activation in the presence of an autophagic flux inhibitor. HEK293T cells were pre-treated without/with Bafilomycin A1 (100 nM Baf for 2 hours) followed by OA (100 nM and 175 nM for 3 hours) and rapamycin (100 nM for 2 hours). (A) The autophagy (LC3, p63) markers were followed by immunoblotting. GAPDH was used as loading control. (B) Densitometry data represent the intensity of LC3II and p62 normalized for GAPDH. For each of the experiments, three independent measurements were carried out. Error bars represent standard deviation asterisks indicate statistically significant difference from the control: ns – nonsignificant; * - p < 0.05; ** - p < 0.01. Figure taken from our previous work [54].

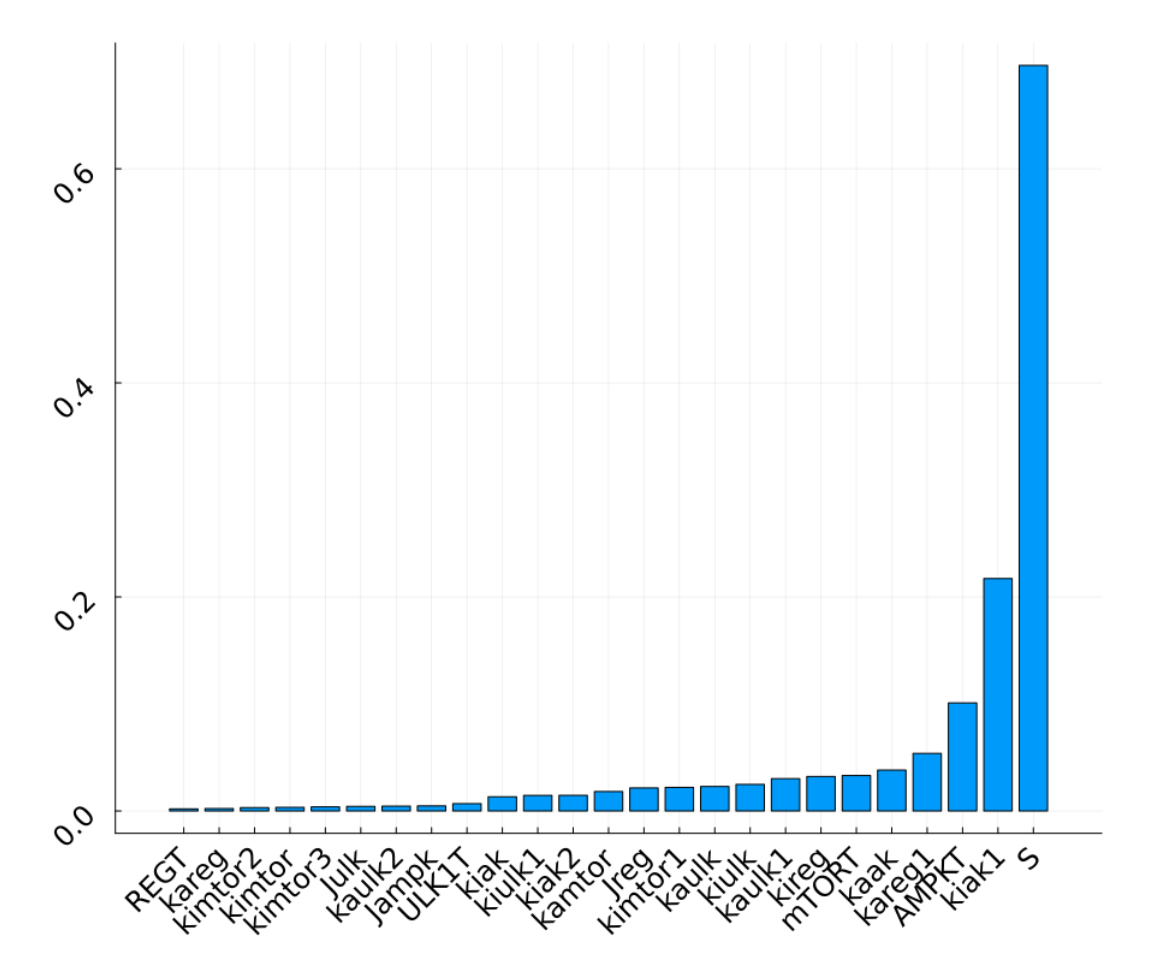


Figure S5: Total Sobol indices of ULK1 model output. The results suggest that the stress level has the most impact on the ULK1 levels (parameter denoted with S. Then the AMPK inhibition by ULK1 (kiak1), total possible AMPK levels (AMPKT) and the activation of REG by AMPK (kareg1). Figure taken from our previous work [141].

Basal model details

The calculations were carried out in $\frac{mol}{cm^3}$, thus the rate coefficients values for the first and second order reactions are taken in $\frac{1}{s}$ and $\frac{cm^3}{mol*s}$ units, respectively [142].

$$DS + P53 \xrightarrow{k1} P53A + DS$$

$$P53A \xrightarrow{k3} MDM2 + P53A$$

$$MDM2 \xrightarrow{k5} \varnothing$$

$$MDM2 + P53A \xrightarrow{k7} MDM2$$

$$P53A + BAX \xrightarrow{k9} BAXA + P53A$$

$$P53A \xrightarrow{k11} P53A + BAX$$

P53A + BCL2
$$\frac{k13}{k15}$$
 P53A_BCL2

BCL2 + BAX $\frac{k17}{k19}$ BCL2_BAX

BAXA $\frac{k21}{k23}$ BAX

BAXA $\frac{k23}{k25}$ \varnothing

BAXA + CYTCM $\frac{k25}{k29}$ BAXA + CYTC

UVG + BAX $\frac{k27}{k29}$ UVG_BAX

CALPAINA + BID $\frac{k31}{k33}$ \varnothing
 \varnothing $\frac{k35}{k35}$ BID

TBID + CYTCM $\frac{k37}{k39}$ TBID + CYTC

CYTC $\frac{k39}{k35}$ \varnothing

CYTC + PROCASP $\frac{k41}{k35}$ CCASP

CASP + BID $\frac{k45}{k35}$ TBID + CASP

CASP + BID $\frac{k47}{k35}$ TBID + CASP

DS + DAPK $\frac{k47}{k39}$ DAPK

P53A + AMPKA $\frac{k51}{k39}$ DAPK

P53A + AMPKA $\frac{k51}{k39}$ P53A + AMPK

P53A + BCL2 $\frac{k55}{k57}$ BCL2_PUMA

PUMA + BCL2 $\frac{k55}{k57}$ BCL2_PUMA

PUMA $\frac{k59}{k39}$ \varnothing

DAPKA + BEC1_BCL2 $\frac{k61}{k65}$ TG_SERCA

CA2IC + SERCA $\frac{k63}{k65}$ TG_SERCA

CCH + PLCE $\frac{k69}{k30}$ PLCEA

EPACA + PLCE $\frac{k71}{k30}$ EPACA + PLCEA

$$IP3R + IP3 \xrightarrow[k77]{k79} IP3R_IP3$$

$$CA2ER + IP3R_{IP3} \xrightarrow[k81]{k81} CA2IC + IP3R_IP3$$

$$IP3R_IP3 + PHAG \xrightarrow[k83]{k85} IP3R_IP3$$

$$IP3 \xrightarrow[k85]{k85} PIP2$$

$$CA2IC + CAMKKB \xrightarrow[k87]{k87} CA2IC + CAMKKBA$$

$$AMPK + CAMKKBA \xrightarrow[k89]{k89} AMPKA + CAMKKBA$$

$$CA2IC + CALPAIN \xrightarrow[k91]{k91} CA2IC + CALPAINA$$

$$CALPAINA \xrightarrow[k93]{k93} CALPAIN$$

$$CALPAINA + GA \xrightarrow[k95]{k99} AC_GAA$$

$$AC_{GAA} \xrightarrow[k101]{k103} \varnothing$$

$$CAMP + EPAC \xrightarrow[k105]{k107} EPAC$$

$$GAA \xrightarrow[k107]{k103} GA$$

$$GABC + GPCRA \xrightarrow[k111]{k111} GAA + GBC + GPCRA$$

$$GA + GBC \xrightarrow[k115]{k111} GAA + GBC + GPCRA$$

$$GA + GBC \xrightarrow[k115]{k111} MTOR_RAP$$

$$RAP + MTORA \xrightarrow[k123]{k112} MTOR_RAP$$

$$AMPKA + MTORA \xrightarrow[k123]{k123} AMPKA + MTOR$$

$$MTORA + AMPKA \xrightarrow[k123]{k123} MTORA + AMPK$$

$$ULKA + MTORA \xrightarrow[k123]{k123} MTORA + ULK$$

$$ULKA + MTORA \xrightarrow[k131]{k123} MTOR + ULKA$$

$$AMPKA + TSC \xrightarrow[k133]{k135} RHEB + TSCA$$

$$RHEBA + TSCA \xrightarrow[k135]{k137} RHEBA + MTORA$$

RHEB
$$\stackrel{k139}{\longrightarrow}$$
 RHEBA

AKTA $\stackrel{k141}{\longrightarrow}$ AKT

AKTA + TSCA $\stackrel{k143}{\longrightarrow}$ AKTA + TSC

ATG5T + BCL2 $\stackrel{k145}{\longrightarrow}$ ATG5_BCL2

CALPAINA + ATG5 $\stackrel{k149}{\longrightarrow}$ CALPAINA + ATG5T

CALPAINA + BEC1 $\stackrel{k151}{\longrightarrow}$ CALPAINA

IP3R + BCL2 $\stackrel{k153}{\longrightarrow}$ IP3R_BCL2

BEC1 + BCL2 $\stackrel{k157}{\longrightarrow}$ BEC1_BCL2

ULKA $\stackrel{k161}{\longrightarrow}$ ULKA + PHAG

AMPKA + ULK $\stackrel{k163}{\longrightarrow}$ AMPKA + ULKA

AMPK + NS $\stackrel{k165}{\longrightarrow}$ AMPKA + NS

AMPKA $\stackrel{k167}{\longrightarrow}$ AMPK

ULKA $\stackrel{k169}{\longrightarrow}$ ULK

AMPKA + ULKA $\stackrel{k171}{\longrightarrow}$ AMPK + ULKA

PHAG + BEC1 $\stackrel{k173}{\longrightarrow}$ PREAUT + BEC1

PHAG + BEC1_UVG $\stackrel{k175}{\longrightarrow}$ PREAUT + BEC1_UVG

 \varnothing $\stackrel{k181}{\Longrightarrow}$ BEC1

PHAG $\stackrel{k183}{\longrightarrow}$ \varnothing

ATG5 + PHAG $\stackrel{k183}{\longrightarrow}$ \varnothing

ATG5 + PHAG $\stackrel{k185}{\longrightarrow}$ ATG5 + AUT

AUT $\stackrel{k187}{\longrightarrow}$ \varnothing

AUT + NS $\stackrel{k199}{\longrightarrow}$ AUT

AUT + DS $\stackrel{k191}{\longrightarrow}$ AUT

 \varnothing $\stackrel{k193}{\longrightarrow}$ PHAG

PREAUT $\stackrel{k195}{\longrightarrow}$ \varnothing

P53A $\stackrel{k197}{\longrightarrow}$ P53A + DRAM

DRAM $\xrightarrow{k199} \emptyset$

Table S1: List of the species found in the models, and their full names [142].

Short Notation	Full Name
AMPK	AMP-activated protein kinase
nS	Nuclear Stress
AMPKa	Active AMP-activated protein kinase
mTORa	Active mammalian target of rapamycin
mTOR	mammalian target of rapamycin
mTOR_ULK	mTOR ULK complex
ULKa	Active Unc-51 like autophagy activating kinase
ULK	Unc-51 like autophagy activating kinase
phag	Phagophore
TSC	Tuberous sclerosis complex
TSCa	Active tuberous sclerosis complex
RHEBa	Active Ras homolog enriched in brain
RHEB	Ras homolog enriched in brain
BEC1	Beclin-1
preAUT	Pre-autophagosome
BEC1_UVG	Beclin-1 UVRAG complex

Table S1: List of the species found in the models, and their full names [142].

Short Notation	Full Name
UVG	UV radiation resistance-associated gene
BEC1c	Cytosolic Beclin-1
cytc	Cytochrome c
ATG5	Autophagy-related protein 5
AUT	Autophagosome
eS	ER Stress
PERK	Protein kinase R-like endoplasmic reticulum kinase
PERKa	Active PERK
ATF4a	Active Activating Transcription Factor 4
ATF4	Activating Transcription Factor 4
dS	DNA Stress
DAPK	Death-associated protein kinase
DAPKa	Active death-associated protein kinase
EPACa	Active exchange protein directly activated by cAMP
PLCe	Phospholipase C epsilon
PLCea	Active phospholipase C epsilon
PIP2	Phosphatidylinositol 4,5-bisphosphate
IP3	Inositol trisphosphate
Ca2er	Endoplasmic reticulum calcium ion
IP3R_IP3	IP3 receptor IP3 complex
Ca2ic	Intracellular calcium
SERCA	Sarcoplasmic/endoplasmic reticulum calcium ATPase
Bax	Bcl-2-associated X protein
Baxa	Active Bcl-2-associated X protein
IP3R	IP3 receptor
IP2	Inositol bisphosphate
IP	Inositol phosphate
Ins	Insulin
CaMKKb	Calcium/calmodulin-dependent protein kinase kinase beta
CaMKKba	Active calcium/calmodulin-dependent protein kinase kinase b
BCL2	B-cell lymphoma 2
IP3R_BCL2	IP3 receptor BCL2 complex
BEC1_BCL2	Beclin-1 BCL2 complex
BCL2p	Phosphorylated BCL2
Calpain	Calpain

Table S1: List of the species found in the models, and their full names [142].

Short Notation Full Name

Calpaina Active calpain

Ga G protein alpha subunit

Gaa Active G protein alpha subunit

ATG5t truncated ATG5

ATG5_BCL2 ATG5 BCL2 complex

Bid BH3 interacting-domain death agonist

tBid Truncated Bid
AC Adenylate cyclase

AC_Gaa Adenylate cyclase G protein alpha subunit complex

cAMP Cyclic adenosine monophosphate

EPAC Exchange protein directly activated by cAMP

G G protein

AC_Ga Adenylate cyclase G protein alpha subunit complex

Gabg G protein alpha, beta, gamma subunits
GPCRa Active G protein-coupled receptor
Gbg G protein beta and gamma subunits

BCL2_Bax BCL2 Bax complex p53m Mitochondrial p53 UVG_Bax UVG bound to Bax

caspase Procaspase

caspasea Cleaved caspase

JNKa Active c-Jun N-terminal kinase

p53c Cytosolic p53 p53a Active p53

Mdm2 Mouse double minute 2 homolog

p53_BCL2 p53 BCL2 complex

DRAM DNA damage-regulated autophagy modulator

PUMA p53 upregulated modulator of apoptosis

PUMA BCL2 PUMA BCL2 complex

TFEBi Inactive transcription factor EB

TFEB Transcription factor EB
PI3K Phosphoinositide 3-kinase

PI3Ka Active phosphoinositide 3-kinase

AKT Protein kinase B

AKTa Active protein kinase B

Table S1: List of the species found in the models, and their full names [142].

Short Notation	Full Name
JNK	c-Jun N-terminal kinase
MAPK15	Mitogen-activated protein kinase 15
MAPK15a	Active mitogen-activated protein kinase 15
PKA	Protein kinase A
PKAa	Active protein kinase A

Initial protein concentrations

Table S2: Initial species concentration ranges in nM [142]

AC 100 400 [161, 162] AC_Ga 0 100 assumed AC_Gaa 0 100 assumed AKT 0 100 [163, 164] AKTa 50 200 [163, 164]	
AC_Gaa 0 100 assumed AKT 0 100 [163, 164]	
AKT 0 100 [163, 164]	
,	
AKTa 50 200 [163, 164]	
AMPK 187.5 750 [130, 165]	
AMPKa 0 100 [130, 165]	
ATG5 100 400 [166]	
ATG5_BCL2 0 100 assumed	
ATG5t 15 60 assumed	
AUT 0 100 [167]	
BCL2 25 100 [168, 169]	
BCL2_Bax 10 40 [168]	
BCL2_PUMA 25 100 [168]	
BEC1 50 200 [133]	
BEC1_BCL2 0 100 assumed	
BEC1_UVG 0 100 assumed	
Bax 10 40 [168, 169]	
Baxa 0 0 [168, 169]	
Bid 10 40 [168, 169]	
Ca2er 500 2000 [170, 171,	172]
Ca2ic 50 200 [170, 171,	172]
CaMKKb 50 200 [170]	

CaMKKba	0	100	[170]
Calpain	10	40	[173]
Calpaina	0	100	[173]
DAPK	50	200	[133]
DAPKa	0	100	[133]
DRAM	0	100	[133]
EPAC	5	20	assumed
EPACa	0	100	assumed
GPCRa	5	20	[174]
Ga	5	20	[174, 175, 171]
Gaa	0	100	[174, 175, 171]
Gabc	0	100	[174, 175, 171]
Gbc	5	20	[174, 175, 171]
IP3	65	260	[170]
IP3R	5	20	[170]
IP3R_BCL2	0	100	assumed
IP3R_IP3	0	100	assumed
MDM2	0	100	[176, 177]
P53a_BCL2	0	100	assumed
PLCea	0	100	[170]
PLCe	5	20	[170, 172, 178]
PIP2	250	1000	[170]
PKA	75	300	[162]
PKAa	0	100	assumed
PUMA	0	100	assumed
RHEB	0	100	assumed
RHEBa	150	600	assumed
SERCA	0	100	[170]
TSC	112.5	450	[130, 165]
TSCa	0	100	[130, 165]
ULK	35	140	[167]
ULKa	0	100	assumed
UVG	50	200	assumed
UVG_Bax	0	100	assumed
cAMP	0	100	[161, 162]
casp	0	0	assumed
cytc	0	100	[168, 169]

cytcm	10	40	[168, 169]
mTOR	0	100	[130, 133]
mTORa	187.5	750	[130, 133]
mTORa_ULK	0	100	assumed
mTORa_ULKa	0	100	assumed
p53	12.5	50	[176, 177]
p53a	0	100	assumed
phag	0	100	assumed
preAUT	0	100	assumed
procasp	12	48	[168, 179]
tBid	0	100	[168]